University of Nottingham
UK | CHINA | MALAYSIA

PhD Second Year Report

Finite Element Methods for Placental Haemodynamics

Adam M Blakey *Supervised by* ***Reuben D O'Dea, Matthew E Hubbard, Paul Houston***

14th July 2022

This report highlights how we model maternal blood flow in the human placenta, including simulations on representative sub- and whole-placenta geometries. We also detail how we have made progress to validating our model with real-world MRI data, modelled the transport of nutrients, and some details on future research plans.

Contents

Note to reader: there is a supplementary website available with links to higher-resolution images and animations. Please take a look for those figures that require this! https://phd2.blakey.family/

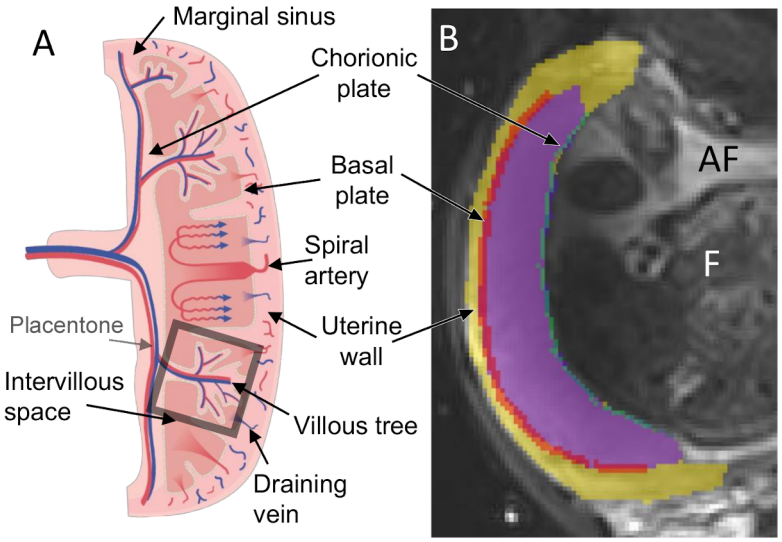

Figure 1: *(A) Schematic showing flow of both maternal and fetal blood through the placenta. Fetal blood flows through fetal vessels in the chorionic plate (left side of diagram) to the villous tree, and returns along the same route. Maternal blood flows through spiral arteries into the intervillous space, and exits via the draining veins. (B) Typical placental MRI image with the purple region corresponding to the placental region of interest. Figure taken from [5], with an added label for a placentone.*

1. Introduction

The placenta is a vital organ to which we were all once attached; without it, we would never have been born. It is also one of the very few organs that can be held in one's hand before the patient is deceased, allowing for some perfusive experiments to be easily performed ex-vivo [1, 2]. Jensen and Chernyavsky explain the role and modelling techniques of the placenta eloquently in [3]. In summary, the placenta has two main purposes: to transport both oxygen and nutrients from mother to fetus, and conversely transport carbon dioxide and waste products from fetus to mother. In human placentas, fetal blood flows through trees consisting of many small villi that are submerged in maternal blood. Maternal blood flows through the intervillous space (IVS), which contains the fetal villous tree; the fetal and maternal blood avoid mixing with each other, and hence the delivery of dissolved nutrients in the blood is transported by diffusion through the large surface area of the villous trees. Each tree is somewhat localised into a region called a placentone, and each placentone may have some number of maternal arteries and veins attached. Placentones are partially separated from neighbouring placentones by septa (or walls), with perhaps 40 to 60 placentones making up the entire placenta [4]. Figure 1 (A) illustrates the above description; Figure 1 (B) shows a typical magnetic resonance imaging (MRI) scan of the placenta.

There has been little attempt at fully-coupled transport models describing both fetal and maternal flow simultaneously [3]; instead, most current models consider either the fetal or maternal blood flow in isolation. In this report we will also consider the maternal flow independently of the fetal flow, but this is a clear limitation of current approaches.

On the fetal side, Plitman Mayo et al. and Kato, Oyen, and Burton have studied transport of nutrients through an individual villi from maternal to fetal blood [6], with Kato, Oyen, and Burton studying also the effect of actively contracting villous trees on maternal blood flow [7]. Clark et al. created a multiscale model of the fetal villous tree and studied how transport of nutrients to fetal blood was affected by changes to the structure of the tree [8].

On the maternal side, current models for flow mostly fall into two main categories: resolving the villous tree precisely — for example through using real-world scan data to simulate on the geometry exactly [9] — or homogenising the tree structure to model the maternal placental blood flow as porous flow [9, 10, 11]. This involves treating the villous tree structure of the fetal vasculature as the 'solid medium' of some permeability, k, and allowing the maternal blood to flow with some resistance through

the gaps in this medium. Whilst Lecarpentier et al. report that the resolved villous tree model gave more realistic results than their homogenised model, they have to resort to solving the nonlinear Navier-Stokes equations, which adds computational complexity, as well as the need to pre-process the scanned images from which to create a computational domain [9]. Some authors that use homogenised models make further modelling enhancements such as varying the permeability throughout the domain [9, 10], or modelling the effect of artery widening before the maternal blood enters the IVS — and what effect this has on placental development [12, 13, 14]. Exchange from mother to fetus is also an important aspect to study, for which the flow of blood can be regarded as a vehicle in which to transport nutrients and waste products; nutrients are transported from mother to fetus, and are what the fetus needs to develop; waste products are also transported, but instead from fetus to mother. Chernyavsky et al. have studied nutrient transport in the placenta from mother to fetus [15], gaining insight into optimal position of veins to maximise transport [11]. Little is known about the rheology of blood in the IVS when compared to blood rheology in narrow capillaries, which have been well-characterised experimentally, and instead many authors model maternal blood flow in the IVS as incompressible [11].

As noted in [3], the described approaches for maternal haemodynamics are mostly restricted to single placentones; Jensen and Chernyavsky further note that there is meaningful progress still to be made at the whole-organ level, and with validating models against experimental data. Furthermore, the exact number of veins in a placenta may vary from placenta-to-placenta, and even from placentone-to-placentone; Chernyavsky, Jensen, and Leach quote estimates of 50–200 veins in the placenta [11]. A standard model has been to allocate one artery and two veins to each artery, and therefore current placental models fail to capture the effects of the marginal sinuses, which are not localised to single placentones — instead located at where the basal plate meets the chorionic plate. The marginal sinus is thought to form a larger outlet than other veins found in the placenta, and has been observed to be surrounded by muscular walls, possibly to control blood flow.

The placental tissue lacks stiff supporting inner structures, and so a poroelastic description may prove appropriate; however, most organ-scale models have assumed fixed tissue geometry [3]. Despite this, there are many other biological applications that take into account elastic effects on geometries; for instance in the lung Pybus et al. model precision-cut lung-slice stretching experiments, making use of biomechanical properties to model the stretching [16], whilst Breen et al. develop a nonlinear elastic law to be representative of the entire lung's behaviour [17]. In addition to dynamics that could arise directly from maternal and fetal blood flow, there are several other forms of movement, such as contractions of the villous tree; Farley, Graham, and Smith document the properties of such phenomena [18], for which Kato, Oyen, and Burton developed an active contraction model for the villous tree and discussed how this may assist blood flow on both the maternal and fetal side [7]; however, the contractions happen simultaneously everywhere, and assumes perfect bifurcations of villous branches. Another form of contraction are the Braxton Hicks contractions, but these contractions involve the entire uterus (as opposed to only the placenta contracting) [19]. However, the newly-documented 'utero-placental pump' phenomenon is a contraction involving only the placenta [5]; Dellschaft et al. report that it has been found experimentally that placental volume can reduce by up to 40% in these 'utero-placental pump' contractions over a 10-minute period, resulting in a periodic ejection of blood from the IVS. The utero-placental pump is a distinct phenomenon to the previously described contractions, and as such should be modelled appropriately. The cause of these contractions is currently unknown, but there may already exist mathematical models in the literature that could be utilised to model this behaviour. For example, we may be able to reapply the work of Collis et al. [20] to accurately model the fluid-structure interaction (FSI) that arises between the maternal blood in the IVS with the surrounding contracting tissue, as well as their coupled nutrient transport problem.

FSI problems are, perhaps obviously by their name, associated with the interaction between fluids and solids (or structures), and can arise in many areas including the aeroelasticity of aircraft wings [21], the playing of reeded woodwind instruments [22], the construction of bridges [23], and the haemodynamics of other animals [24]. In terms of numerical simulations of fluid-structure interaction problems, there are generally two approaches: the monolithic approach, and the partitioned approach. The former treats the fluid and structure dynamics in the same mathematical framework and is solved

simultaneously by a unified algorithm, and the latter treats the fluid and structure as two separate fields — which can be solved separately with their own meshes and numerical algorithms — and can be useful when using 'legacy' codes that have already been validated for solving many complicated problems [25]. The vast existing literature on these types of problems may be beneficial for application to placental haemodynamics.

For the numerical simulations undertaken here, we employ finite element methods (FEMs) as our numerical method of choice — and more specifically, we use discontinuous Galerkin finite element methods (DGFEMs). Another option would have been to use continuous Galerkin finite element methods (CGFEMs), which differ to DGFEMs by enforcing continuity between 'elements' in each computational mesh. Loosely speaking, DGFEMs are somewhat of a hybrid between classical continuous FEMs and finite volume methods (FVMs) [26], the latter being used extensively in computational fluid dynamics (CFD) simulations. Cangiani et al. [26] highlight that DGFEMs are a great choice for modelling in many practical settings due to their simple treatment of complicated geometries, ease of adaptivity in both the local mesh subdivision and local polynomial degree, and availability of rigorous error analysis tools. A posteriori tools are of particular practical interest for both error quantification as well as automatic adaptivity strategies. DGFEMs in particular are highly parallelisable from a computational viewpoint as elements only involve communication across element faces, allowing some computations to take place independently of each other, i.e. in parallel [27]. We note that we specifically use the DGFEM symmetric interior penalty method which is both consistent and stable [28]. DGFEMs form a natural choice of method for our application due to the inherent complicated placental geometries, as well as the use of local adaptivity for reducing computational efforts.

The problem we aim to address is concerned with diseases, such as fetal growth restriction (FGR) and early-onset pre-eclampsia, which are thought to be associated with spiral arteries failing to widen as they enter the IVS [12]; this is usually called 'conversion', for which Figure 2 from [12] illustrates the widening effect in a normal pregnancy. However, the resolution of typical MRI scanners are too large to accurately detect phenomena on the scale of a single artery (the MRI scanner used in [5, Tab. S3] has a resolution of $2.5\,\text{mm} \times 2.5\,\text{mm} \times 6\,\text{mm}$, but typical spiral artery openings are approximately of size 2 mm, or even smaller in pre-eclamptic cases, as shown in Figure 2). With current MRI technology, accurate study of the maternal haemodynamics is deferred to mathematical modelling and prediction; from which, we can further study the transport of vital nutrients such as oxygen, as reduced nutrient transport has been shown to affect the development or cause premature death of fetuses. We are therefore aiming to develop a mathematical model to simulate maternal blood flow and nutrient transport phenomena at and below the resolution of typical MRI scanners, whilst including accurate modelling of new phenomena such as the 'utero-placental pump', and validate our findings by comparing the simulated dynamics on the organ-scale to real-world MRI data and ex-vivo perfusion data. The hope is that this work will lead to better understanding of these diseases, and therefore ultimately lead to improved pregnancy outcomes.

The structure for the remainder of this report is as follows. Section 2 we will model the flow of maternal blood in the IVS, treating the IVS as a porous medium. In Section 3 we will undertake simple simulations at the placentone- and placenta-level, and then in Section 4 use a new technique to artificially recreate MRI data for comparison; in Sections 5.1–5.3 we will make short introduction to work to follow on septal walls, nutrient transport, and variable permeability, respectively. We end this report in Section 6 with some conclusions and a plan of what we hope to accomplish in the coming year. We outline a summary of official training undertaken in Appendix A, and outline an approximate work timeline for the next 12 months in Appendix B.

2. Blood Flow Modelling

We assume that the flow of maternal blood through this porous medium is governed by the incompressible Darcy-Brinkman equations, similarly to Lecarpentier et al. in their Model 1 [9].

Poromechanics more generally describes the behaviour of fluids saturating porous media, where the fluid may be a liquid or a gas, and the structure is generally solid [20] — although there are models

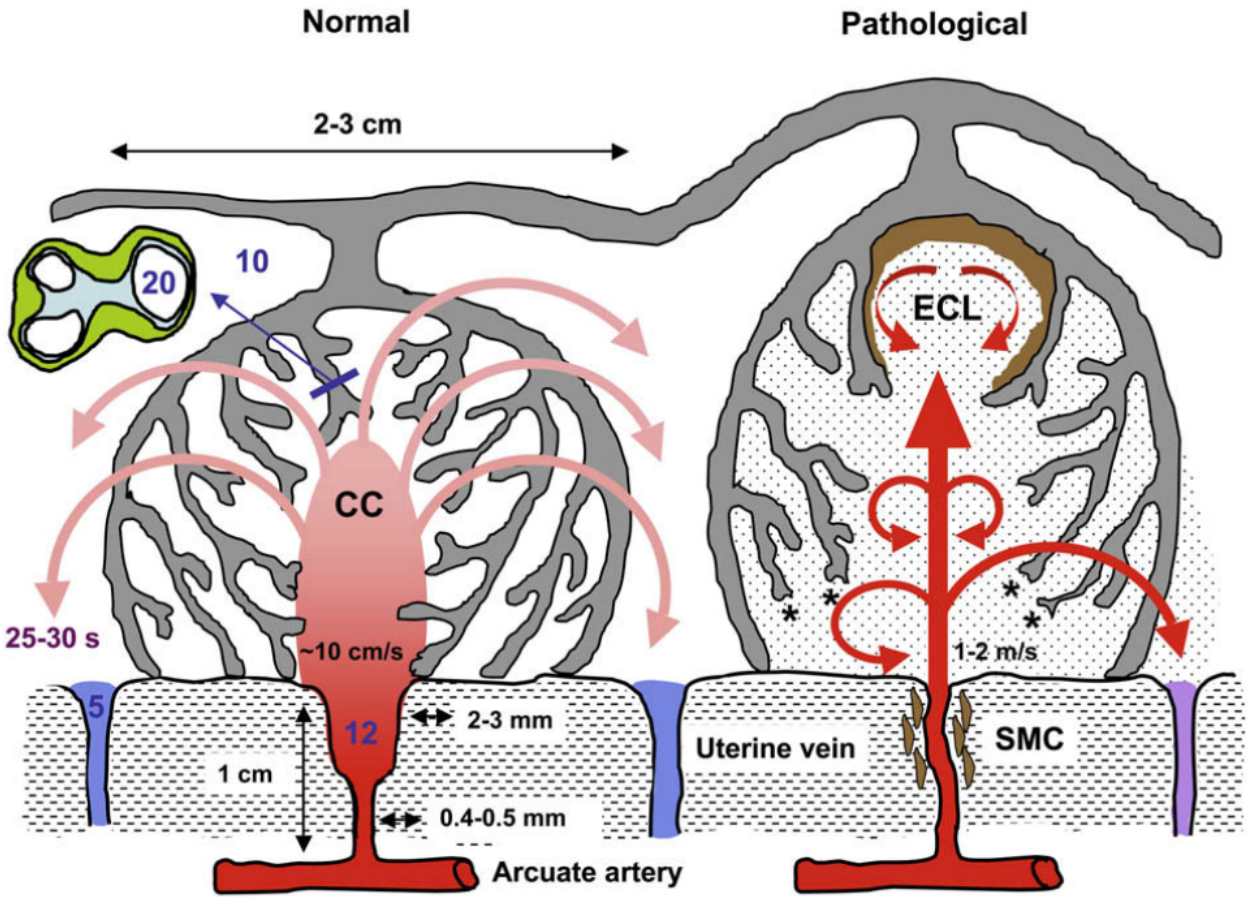

Figure 2: *Diagram illustrates, among other things, the central cavity (shown as CC) in relation to the villous tree (shown in grey). A typical placentone is shown on the left and a pathological placentone is shown on the right. Figure taken from [12].*

that make the structure permeable or elastic. The simplest example of steady, incompressible flow through a porous medium is Darcy's law. For an open and bounded domain $\Omega \subset \mathbb{R}^d$, for $d = 2, 3$, Darcy's law is given by

$$\boldsymbol{\nabla} \cdot \mathbf{u} = 0 \text{ in } \Omega, \tag{1a}$$

$$\mathbf{u} = -\frac{k}{\mu}\boldsymbol{\nabla} p \text{ in } \Omega, \tag{1b}$$

where $\mathbf{u}$ is the vector velocity field of the fluid, p is the scalar pressure field, k is permeability (simply, it is related to the inverse of flow resistance [11]), and μ is the viscosity of the fluid. We have omitted boundary conditions here for ease of presentation.

A modification to Darcy's law was made by Brinkman in 1949. The modification is the addition of a diffusion term, which captures additional inertial effects. We choose the Darcy-Brinkman model for modelling the dynamics of maternal blood flow through the IVS.

Taking $\partial\Omega$ to denote the $(d-1)$-dimensional boundary of Ω, we partition the boundary into two disjoint sets: Γ_D and Γ_N, which respectively correspond to the regions where we will apply Dirichlet and Neumann conditions; we note the restrictions that $\Gamma_D \neq \emptyset$ and $\Gamma_N := \partial\Omega \setminus \Gamma_D$. Our dimensional Darcy-Brinkman equations with zero external forcing are given by: find $\mathbf{u}$ and p such that

$$-\mu\boldsymbol{\nabla}^2\mathbf{u} + \boldsymbol{\nabla} p + \tilde{\mu}\alpha^2\mathbf{u} = \mathbf{0} \text{ in } \Omega, \tag{2a}$$

$$\boldsymbol{\nabla} \cdot \mathbf{u} = 0 \text{ in } \Omega, \tag{2b}$$

$$\mathbf{u} = \mathbf{g_D} \text{ on } \Gamma_D, \tag{2c}$$

$$(\boldsymbol{\nabla}\mathbf{u} - p\underline{\underline{I}}) \cdot \mathbf{n} = \mathbf{g_N} \text{ on } \Gamma_N, \tag{2d}$$

where $\mathbf{g_D}$ and $\mathbf{g_N}$ are functions of the spatial coordinates, μ is the dynamic viscosity, $\tilde{\mu}$ is the effective viscosity, $\alpha^{-2} = k$ is the permeability, and $\mathbf{n}$ is the usual outward unit normal on Γ_N. We make a simplification to this and take $\tilde{\mu} := \mu$, [30, p. 216]. We nondimensionalise by picking the following scalings: $\mathbf{x} \to L\mathbf{x}$, $\mathbf{u} \to U\mathbf{u}$, $p \to \frac{\mu U}{L}p$; where L is the length-scale, and U is the velocity-scale, which are dependent upon the problem. Note that we also appropriately nondimensionalise our domain Ω and boundary conditions.

Making the simplification of $\mu = \tilde{\mu}$, setting $\alpha^{-2} = k$, and substituting for the nondimensionalised variables, we arrive at our nondimensional Darcy-Brinkman equations: find $\mathbf{u}$ and p such that

$$-\boldsymbol{\nabla}^2\mathbf{u} + \boldsymbol{\nabla} p + \frac{1}{Dr}\mathbf{u} = \mathbf{0} \text{ in } \Omega, \tag{3a}$$

$$\boldsymbol{\nabla} \cdot \mathbf{u} = 0 \text{ in } \Omega, \tag{3b}$$

$$\mathbf{u} = \mathbf{g_D} \text{ on } \Gamma_D, \tag{3c}$$

$$(\boldsymbol{\nabla}\mathbf{u} - p\underline{\underline{I}}) \cdot \mathbf{n} = \mathbf{g_N} \text{ on } \Gamma_N, \tag{3d}$$

where $Dr := \frac{k}{L^2}$ is the Darcy number that describes ratio of permeability to cross-sectional area, and we again note that the domain, Ω, and boundary conditions, $\mathbf{g_D}$ and $\mathbf{g_N}$, have been appropriately scaled.

To arrive at a DGFEM discretisation of Equation (3), we first need to introduce some FEM-related notation.

2.1. DGFEM Discretisation Notation

Finite element methods are one of many choices of numerical method for solving partial differential equations (PDEs). Finite element methods first appeared with Courant in 1943, where the author used the idea of minimising a functional using linear approximations over subregions, which is fundamental to the formulation required for deriving a finite element method (FEM) [30]. It wasn't until Clough in 1960 when the method was given its name, describing how the methods could be used on models

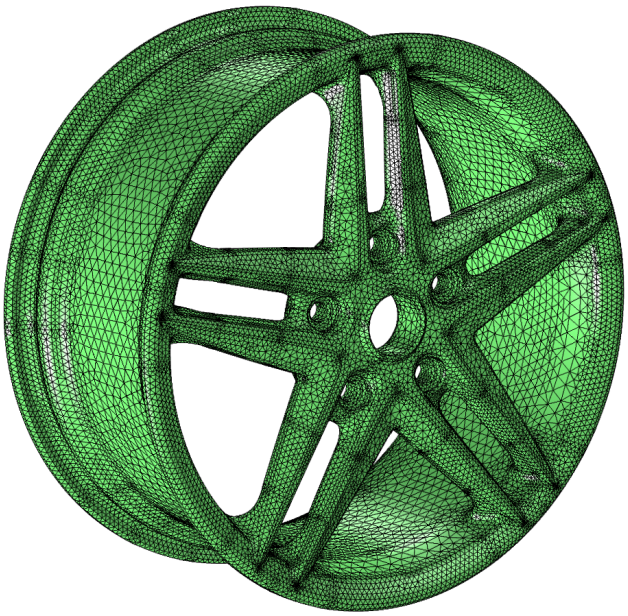

Figure 3: *Diagram illustrates an example 3D mesh using tetrahedral elements. Example taken from https://www.comsol.com/blogs/meshing-your-geometry-various-element-types/ on 2022-07-06 at 10:37 BST.*

of wing structure flexibility at the Boeing Company [31]. The initial development of FEMs are also credited by Gupta and Meek [32] to papers by Argyris [33], Turner et al. [34], and Zienkiewicz [35].

Since the initial work FEMs, many different flavours of FEMs have been developed including the very popular continuous Galerkin FEMs (CGFEMs), discontinuous Galerkin FEMs (DGFEMs) which this work exploits, as well as extended FEMs (XFEMs), cut FEMs (CutFEMs), and *hp*-FEMs — some of which can be combined to make very powerful methods.

As previously mentioned, this work exploits DGFEMs to arrive at our approximated PDE solution; we will not detail the full derivation of the symmetric interior penalty DGFEM method we employ, but we will instead introduce the general idea and some DGFEM-specific notation — full details can be found in [28].

We can take a PDE on some open and bounded domain, $\Omega \subset \mathbb{R}^d, d \in \{2, 3\}$; note that the following notation does not restrict d to just these values, but these are what we will consider for our 2D and 3D simulations. Following [26], we denote the mesh by $\mathcal{T}_h$, which we assume is a shape-regular partition of Ω, which for simplicity consist of non-overlapping d-dimensional open simplicial elements, $\kappa \in \mathcal{T}_h$, such that $\bar{\Omega} = \cup_{\kappa \in \mathcal{T}_h} \bar{\kappa}$, where $\bar{\kappa}$ denotes the closure of κ; an example of a discretised mesh using tetrahedra is shown in Figure 3. Writing $r \in \mathbb{N}_0$ to denote the polynomial degree on a $\kappa \in \mathcal{T}_h$, we introduce the finite element spaces

$$\mathbf{V}_h := \{\mathbf{v} \in L^2(\Omega)^d : \mathbf{v}|_\kappa \in \mathcal{P}_r(\kappa)^d, \kappa \in \mathcal{T}_h\}, \tag{4}$$

$$Q_h := \{q \in L^2(\Omega) : q|_\kappa \in \mathcal{P}_{r-1}(\kappa), \kappa \in \mathcal{T}_h\}, \tag{5}$$

where $\mathcal{P}_r(\kappa)$ denotes the space of polynomials of total degree r on κ, and $L^2(\Omega)$ denotes the space of square-integrable functions on Ω. In words, this notation means that we are seeking numerical approximations to our PDE that are discontinuous piecewise polynomials. We note here that the spaces are chosen such that the pressure space, Q_h, has one lower polynomial degree than the velocity space, $\mathbf{V}_h$; this ensures that the Babuška and Brezzi inf-sup condition is satisfied [36].

As the choice of finite element spaces suggest, DGFEMs admit discontinuities in the approximation of the PDE solution. The DGFEM symmetric interior penalty method we use allows this discontinuity by introducing numerical flux functions, which represents approximations to the flux on the boundaries

of elements; the 'amount' of discontinuity in the method is controlled by a carefully-chosen penalisation parameter, σ. We introduce the notation to describe averages and jumps between adjacent edges. There are two types of faces: interior faces and boundary faces; we write $\mathcal{F}^{\mathcal{I}}$ to denote interior faces between two elements, and $\mathcal{F}^{\mathcal{B}}$ to denote exterior faces that lie on $\partial\Omega$; we set $\mathcal{F} := \mathcal{F}^{\mathcal{B}} \cup \mathcal{F}^{\mathcal{I}}$ and note $\mathcal{F}^{\mathcal{B}} \cap \mathcal{F}^{\mathcal{I}} = \emptyset$.

For both vector and scalar quantities (respectively, $\mathbf{u}$ and p), the average operator defined on an interior face $F = \partial\kappa_i \cap \partial\kappa_j \in \mathcal{F}^{\mathcal{I}}$ between two elements $\kappa_i, \kappa_j \in \mathcal{T}_h$, is given by

$$\begin{aligned}\{\{\mathbf{u}\}\} &:= \frac{1}{2}(\mathbf{u}^+_{\kappa_i} + \mathbf{u}^+_{\kappa_j}),\\ \{\{p\}\} &:= \frac{1}{2}(p^+_{\kappa_i} + p^+_{\kappa_j}),\end{aligned}$$

where $\mathbf{u}^+_{\kappa_i}$ and $p^+_{\kappa_i}$ denote the trace values of $\mathbf{u}$ and p from inside element κ_i, respectively. We may similarly introduce the jump operator on an interior face, $F \in \mathcal{F}^{\mathcal{I}}$, as

$$\begin{aligned}[\![\mathbf{u}]\!] &:= \mathbf{u}^+_{\kappa_i} \cdot \mathbf{n}_{\kappa_i} + \mathbf{u}^+_{\kappa_j} \cdot \mathbf{n}_{\kappa_j},\\ [\![p]\!] &:= p^+_{\kappa_i}\mathbf{n}_{\kappa_i} + p^+_{\kappa_j}\mathbf{n}_{\kappa_j},\end{aligned}$$

where $\mathbf{n}_{\kappa_i}$ and $\mathbf{n}_{\kappa_j}$ denote the outward unit normals to κ_i and κ_j, respectively, on F. Similarly, the average and jump operators on boundary faces, $F \in \mathcal{F}^{\mathcal{B}}$, where $F \subset \partial\kappa_i$, are defined as

$$\begin{aligned}\{\{\mathbf{u}\}\} &:= \mathbf{u}^+_{\kappa_i},\\ \{\{p\}\} &:= p^+_{\kappa_i},\\ [\![\mathbf{u}]\!] &:= \mathbf{u}^+_{\kappa_i} \cdot \mathbf{n}_{\kappa_i},\\ [\![p]\!] &:= p^+_{\kappa_i}\mathbf{n}_{\kappa_i}.\end{aligned}$$

For all simulations in this report, we implement our DGFEM solver using AptoFEM [42], which is a general-purpose finite element method software that permits DGFEM spaces, use of a posteriori error estimation, and interface to extremely fast third party matrix solving packages such as MUMPS [43].

2.2. DGFEM Darcy-Brinkman Discretisation

We take the nondimensionalised Darcy-Brinkman equations in Equation (3) and, by following a similar procedure to [37, Sec. 2.4], we define:

$$\begin{aligned}A(\mathbf{u},\mathbf{v}) &:= \int_\Omega \nabla\mathbf{u} : \nabla\mathbf{v}\,\mathrm{d}\mathbf{x} - \int_{\mathcal{F}^{\mathcal{I}}} (\{\{\nabla\mathbf{v}\}\} : [\![\mathbf{u}]\!] + \{\{\nabla\mathbf{u}\}\} : [\![\mathbf{v}]\!])\,\mathrm{d}s + \int_{\mathcal{F}^{\mathcal{I}}} \sigma[\![\mathbf{u}]\!] : [\![\mathbf{v}]\!]\,\mathrm{d}s + \frac{1}{Dr}\int_\Omega \mathbf{u}\cdot\mathbf{v}\,\mathrm{d}\mathbf{x},\\ B(\mathbf{v},q) &:= -\int_\Omega q\nabla\cdot\mathbf{v}\,\mathrm{d}\mathbf{x} + \int_F \{\{q\}\}[\![\mathbf{v}]\!]\,\mathrm{d}s,\\ L(\mathbf{v}) &:= \int_\Omega f\mathbf{v}\,\mathrm{d}\mathbf{x} - \int_{\Gamma_N} \mathbf{g}_N\mathbf{v}\,\mathrm{d}s + \int_{\Gamma_D} (\mathbf{g_D}\otimes\mathbf{n}) : \nabla\mathbf{v}\,\mathrm{d}s + \sigma\int_{\Gamma_D} \mathbf{v}g_D\,\mathrm{d}s + \int_{\Gamma_D} q\mathbf{g}_D\cdot\mathbf{n}\,\mathrm{d}s,\end{aligned}$$

where $\Gamma_D, \Gamma_N \subseteq \mathcal{F}^{\mathcal{B}}$ denote the boundary faces on the Dirichlet and Neumann boundaries, respectively, $\mathbf{u},\mathbf{v} \in \mathbf{V}_h$ and $p, q \in Q_h$, and $\sigma = 10\frac{r^2}{h}$ is the DGFEM symmetric interior penalty parameter taken from [38] and is computed locally on an element with total degree r and mesh width h.

Our DGFEM discretisation of the nondimensional Darcy-Brinkman equations is given by: find $(\mathbf{u}_h, p_h) \in \mathbf{V}_h \times Q_h$ such that

$$A(\mathbf{u}_h, p_h) - B(\mathbf{v}_h, p_h) + B(\mathbf{u}_h, q_h) = L(\mathbf{v}_h), \tag{6}$$

for all $(\mathbf{v}_h, q_h) \in \mathbf{V}_h \times Q_h$.

2.3. DGFEM A Posteriori Error Estimation and h-adaptivity

A large portion of the first-year report concentrated on how we may use a posteriori error estimation to effectively refine our mesh where it is needed most [39]. In some of the following simulations, where it is required, we will also use a posteriori error indicators to inform which elements to perform h-adaptivity on, which increases the accuracy of our solution whilst keeping the degrees of freedom (DoFs) as low as possible.

An a posteriori error bound takes the form

$$\|u - u_h\| \leq \mathcal{E}(h, r, u_h),$$

where the error bound $\mathcal{E}$ depends only on the mesh size h, polynomial degree r, and the *approximate* solution u_h. This is different to a priori error bounds that instead depend on the *exact* solution, which in practical settings is unknown. Not only does this give us access to bounds on the error without knowing the true solution, it also paves the way for automatic local adaptivity. In this report we will focus specifically on h-adaptivity, where refinement of elements is undertaken in response to the local element error indicators.

Houston, Schötzau, and Wihler give an energy norm a posteriori error bound, from which we can derive an elemental error indicator [37]; they present the analysis for the Stokes problem, which can be easily modified for our Darcy-Brinkman problem from Equation (3) since the additional reaction term contains no derivatives, therefore leaving most of the analysis unchanged. The elemental error indicator for our Darcy-Brinkman problem is given by

$$\begin{aligned}\eta_\kappa^2 =& h_\kappa^2 \left\| \nabla^2 \mathbf{u}_h - \boldsymbol{\nabla} p_h - \frac{1}{Dr}\mathbf{u}_h \right\|_{L^2(\kappa)}^2 + \|\boldsymbol{\nabla}\cdot\mathbf{u}_h\|_{L^2(\kappa)}^2 \\ &+ \left\| \mathrm{h}^{\frac{1}{2}} \left([\![p_h]\!] + \frac{1}{Dr}[\![\mathbf{u}_h]\!] - [\![\nabla \mathbf{u}_h]\!] \right) \right\|_{L^2(\partial\kappa\setminus\partial\Omega)}^2 + \left\| \sigma^2 [\![\mathbf{u}_h]\!] \right\|_{L^2(\partial\kappa)}^2,\end{aligned}$$

for $\kappa \in \mathcal{T}_h$, where $\|\cdot\|_{L^2(\cdot)}$ denotes the L^2-norm on some domain, and

$$\mathrm{h}(\mathbf{x}) = \begin{cases} \min\{h_\kappa, h_{\kappa'}\}, & \mathbf{x} \in F \in \mathcal{F}^{\mathcal{I}},\ F = \partial\kappa \cap \partial\kappa', \\ h_\kappa, & \mathbf{x} \in F \in \mathcal{F}^{\mathcal{D}},\ F \subset \partial\kappa, \end{cases}$$

where h_κ and $h_{\kappa'}$ are respectively the elemental diameters of elements κ and κ'. Whilst we cannot say that η_κ is an upper bound of the error on each individual element, $\kappa \in \mathcal{T}_h$, we can use the indicator to approximately calculate where the error in the solution is largest — and therefore we can automatically decide regions of the mesh to concentrate our computational power, by refining the elements only in those regions where the error indicator is large.

3. Blood Flow Simulations

3.1. Single Placentone

Taking inspiration from Lecarpentier et al. [9], we construct a simple 2D geometry of a single placentone, formed of a rectangle with a semicircle placed on top. From [11] and [9] we know the diameter of a normal full-term placentone is approximately 40 mm and that the widths of the inlets and outlets are approximately 2 mm; we also choose to centre-align the inlet, and take the outlets with 8 mm between their centres and the side walls. This geometry corresponds to a lengthscale $L = 0.04$, and for a typical healthy placenta we have $U = 0.1\,\mathrm{m\,s^{-1}}$ [12]. We add square pipes to the inlet and outlet locations to represent the arteries and veins, governed only by Stokes flow; as there is no villous tree in present in the arteries and veins, we split Ω into two parts: Ω_D and Ω_S, which respectively correspond to regions where we solve Equation 3 and where we solve for Stokes flow. We set Ω_S to contain the inflow and outflow pipes shown at the bottom of Figure 4, and $\Omega_D = \Omega \setminus \Omega_S$; practically-speaking, we simply 'turn

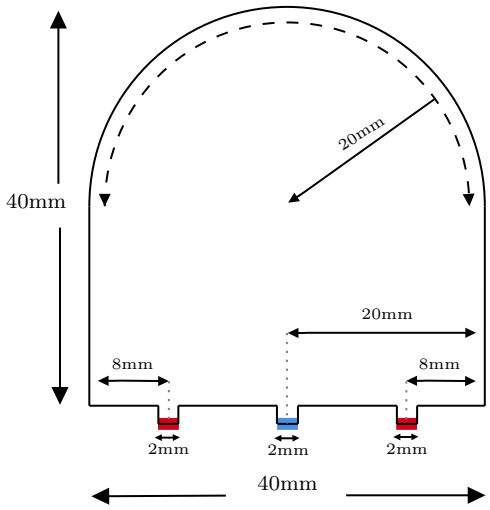

Figure 4: *Diagram illustrates a simple 2D geometry for a single placentone. Blue shows inlet locations and red shows outlet locations.*

off' the zeroth-order reaction term in this region to avoid the need for interfacial conditions between these different PDEs. The motivation for this domain choice is that it roughly corresponds to a 2D slice through a fetal villous tree [11]. A visual representation of the described dimensional geometry is shown in Figure 4.

We take the average permeability from [9] to be $k = 10^{-8}$; this gives $Dr = 1.6 \times 10^5$. We choose the boundary conditions such that there is a Poiseuille parabolic inflow on the inlet — given as

$$\mathbf{g_D}(x) = -\frac{(x - x_L)(x - x_R)}{(x_M - x_L)(x_R - x_M)}\hat{\mathbf{y}}, \tag{7}$$

where x_L, x_M, and x_R respectively denote the left, midpoint, and right x-coordinates of the inlet, and $\hat{\mathbf{y}}$ denotes the unit vector in the y-direction — zero outward flux ($\mathbf{g_N} = \mathbf{0}$), and no slip elsewhere ($\mathbf{g_D} = \mathbf{0}$).

We employ a mesh with refinement near inlets and outlets, ultimately giving 113,448 elements. We choose polynomial degree 2 in the velocity components and polynomial degree 1 in the pressure component, giving the so-called Taylor-Hood elements, which are a stable combination of spaces [40, sec. 8.8], and are one of the mostly widely-used elements for solving Stokes flow [41]. The choice of parameters run with AptoFEM [42] gives the mesh and solution depicted in Figure 5.

The velocity field shown in Figure 5(b) shows that fluid moves from the centre inlet to the two outlets either side. We note that the colouring is logarithmically-scaled, and therefore showing that we roughly have an exponential slowdown of the fluid as it enters the IVS. The nondimensionalisation in Equation (3) is independent of the choice of velocity-scale, U, so the earlier choice of U maps the shown colour bar instead to range from $1 \times 10^{-6}\,\mathrm{m\,s^{-1}}$ to $1 \times 10^{-1}\,\mathrm{m\,s^{-1}}$ in dimensional units. The results here agree with the results obtained by Lecarpentier et al. [9], and Chernyavsky, Jensen, and Leach [11].

3.2. Whole Placenta

A short-coming of single placentone simulations such as those considered in Section 3.1, is that they do not permit transport over septa, i.e. there is no flux of blood between neighbouring placentones, as would be expected in the sub-chorionic space (SCS) [3]. As far as we are aware, there is no published work that tackle simulations of maternal blood flow on the scale of the entire placenta; this section demonstrates simulations of maternal blood flow in the intervillous space (IVS) on a representative 2D slice of a whole human placenta.

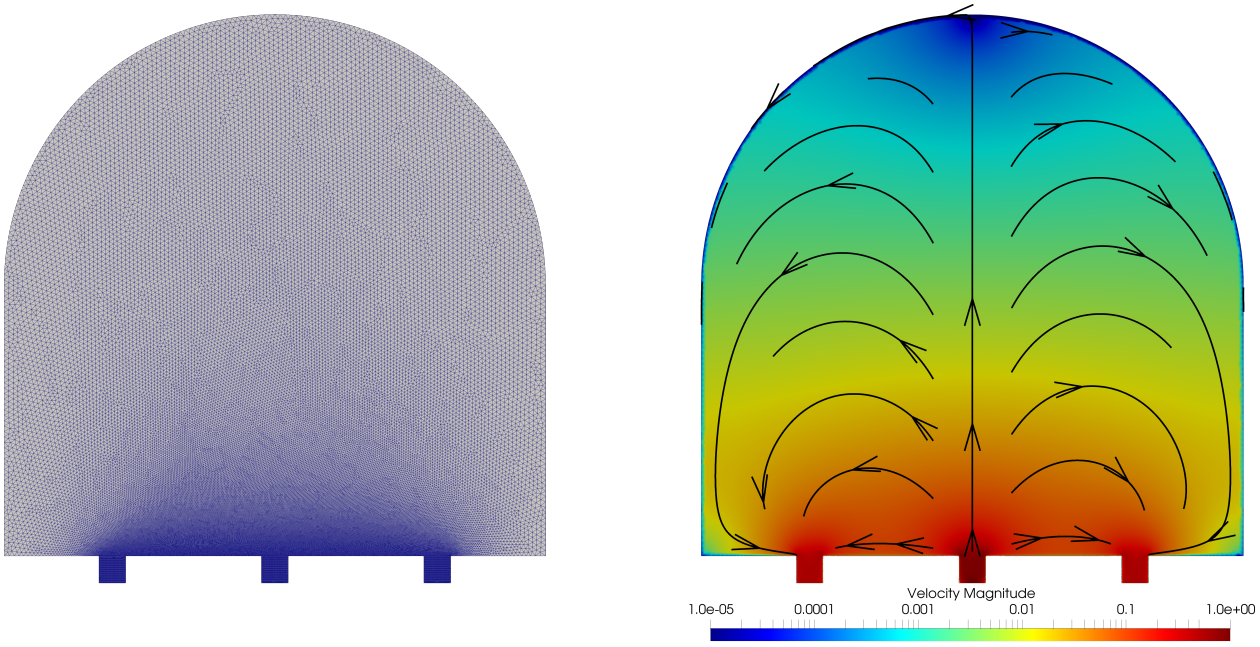

(a) **(b)**

Figure 5: *(a) Mesh of the placentone simulation described in Section 3.1. (b) Plot showing logarithmic velocity magnitude in colour (blue is slow, red is fast) with black streamlines and arrows for the placentone simulation described in Section 3.1.*

Serov et al. report that there are approximately 40–60 placentones in the entire placenta. We estimated that a 2D planar cross-section could contain approximately 6 placentones (assuming a total placental width of approximately 25 cm and placentone width of approximately 4 cm), so we designed a domain to simulate flow in this geometry; we note that this assumes that this cross-section perfectly intersects through the centre of all inlets and outlets, and note that 6 placentones is possibly an underestimate of the true number found in a 2D slice. We assume that there are impermeable walls (septa) of height 24 mm and width 3 mm between placentones, and that the placentones are located on an arc of a circle of centre (x_c, y_c), which is constructed such that the horizontal extremities form a 45°-angle with the x-axis; we note that veins are not just found on the basal plate [44], so we have added two corner outlets of widths 4 mm to the geometry in order to model this additional drainage in each of the corners. This described geometry is illustrated in Figure 6.

We run a simulation with the same boundary conditions as in Section 3.1, namely: parabolic Dirichlet inflow on inlets, Neumann zero on outlets, and Dirichlet zero elsewhere; we note that the parabolic inflow conditions are now normally-oriented, which is to say on the inlets we set

$$\mathbf{g_D}(x) = -\frac{(x-x_L)(x-x_R)}{(x_M-x_L)(x_R-x_M)}\cos(\theta_n)\hat{\mathbf{x}} + \frac{(x-x_L)(x-x_R)}{(x_M-x_L)(x_R-x_M)}\sin(\theta_n)\hat{\mathbf{y}}, \tag{8}$$

where $\hat{\mathbf{x}}$ and $\hat{\mathbf{y}}$ respectively denote the unit vectors in the x- and y-directions, θ_n is the angle between the outward normal and the horizontal. We also employ a similar mesh, that is again more refined near inlets and outlets, giving 955,500 elements. We again choose polynomial degrees $(2, 2, 1)$ respectively for the two velocity components and pressure and implement using AptoFEM [42]. This choice of parameters gives the mesh and solution depicted in Figure 7.

The velocity field in Figure 7(b) shows, like Figure 5(b), that fluid moves within placentones from the inlets to the outlets; the difference now is that these simulations permit transport of fluid between placentones through the sub-chorionic space (SCS). Although the movement between placentones is slow (approximately on the order of 1% of the inlet fluid velocity), it may be an important aspect to study in terms of nutrient transport. We also notice that the corner veins appear to be important in draining fluid from the placenta, shown by the relatively large velocity magnitude there. Interestingly, there appear to be stagnation points not only in the top-centre of the domain, but also in four other

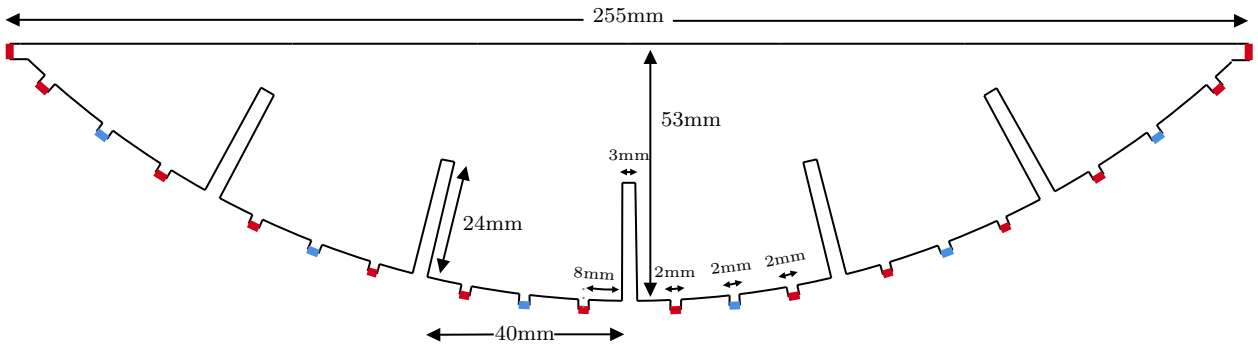

Figure 6: *Diagram illustrates a simple 2D geometry for a slice of the whole placenta, consisting of 6 adjacent placentones. Blue indicates inlet locations and red indicates outlet locations.*

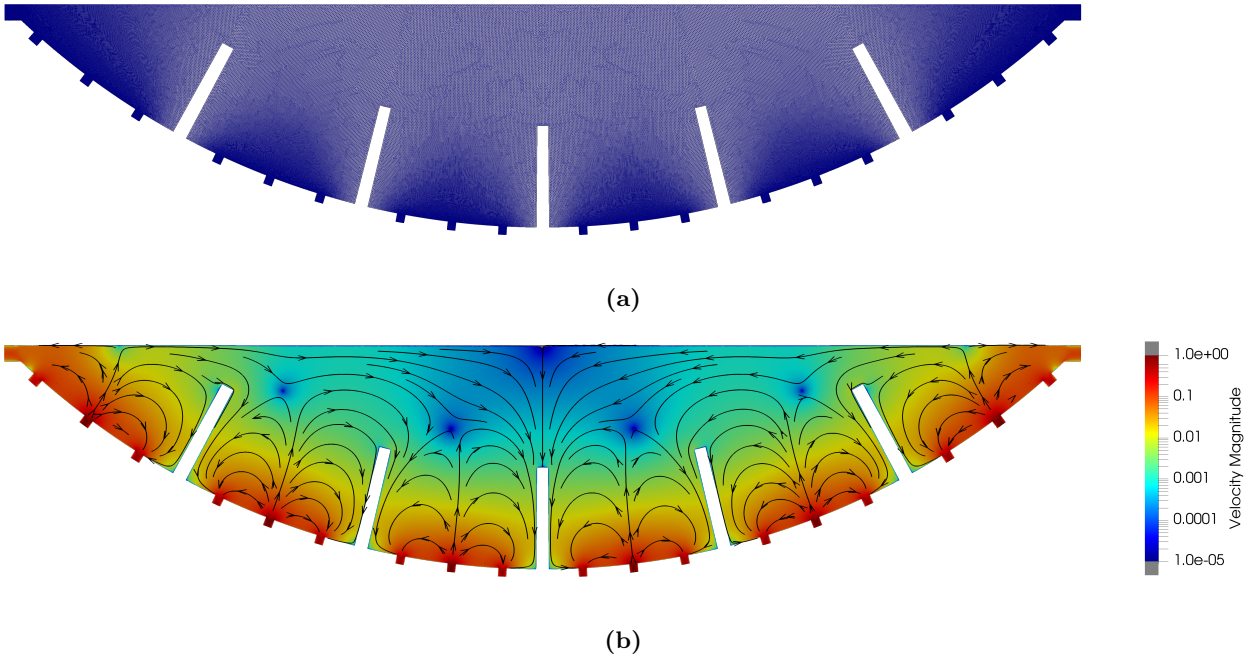

(a)

(b)

Figure 7: *(a) Mesh of the placenta simulation described in Section 3.2. (b) Plot showing logarithmic velocity magnitude in colour (blue is slow, red is fast) with black streamlines and arrows for the placentone simulation described in Section 3.2.*

locations — above four of the placentones — indicated by the blue patches. We note that generally, the fluid velocity is very slow throughout the entire domain, except near inlets and outlets. It is not a given in physical placentas that every placentone has one artery and two veins, nor is it true that every placentone has the same shape and size, but this is an assumption we make for these simple simulations.

Concentrating on a single placentone in this wider whole placentone simulation, the fluid flow in Figure 7(b) similar to the single placentone simulations in figure 5(b). This shows that the single placentone simulations could indeed still be useful for understanding flow in the placenta.

4. MRI and Model Validation

It is, of course, important that we validate our model with real world measurements; we will not provide such a validation in this section, but we will show some progress toward this. Other authors, for example Lecarpentier et al., validated their model by comparing measurements of wall shear stress [9]. We aim to validate our model by comparing synthetically generated MRI data from our simulated flow data with real world MRI data for real placental flows, and ultimately hope to compare with ex-vivo perfusion data (not covered in this report). First, we outline a brief overview of how an MRI scanner makes its measurements.

4.1. An Introduction to MRI Measurements

4.1.1. Voxels

MRI makes use of voxels: 3D boxes, within which MRI makes its measurements. Within each voxel, there are water molecules which each have a magnetic spin associated with them. It is the collective magnetic spin within each voxel that MRI measures . For the simulations we are performing, the voxels are approximately $2.5\,\text{mm} \times 2.5\,\text{mm} \times 6\,\text{mm}$. An example voxel containing some particles is illustrated in Figure 8.

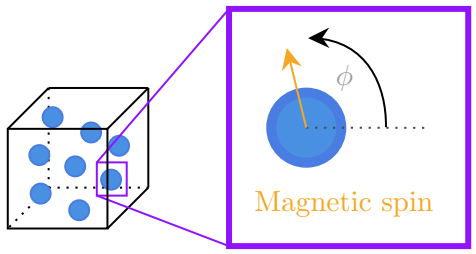

Figure 8: *Diagram illustrates voxels and water molecules within.*

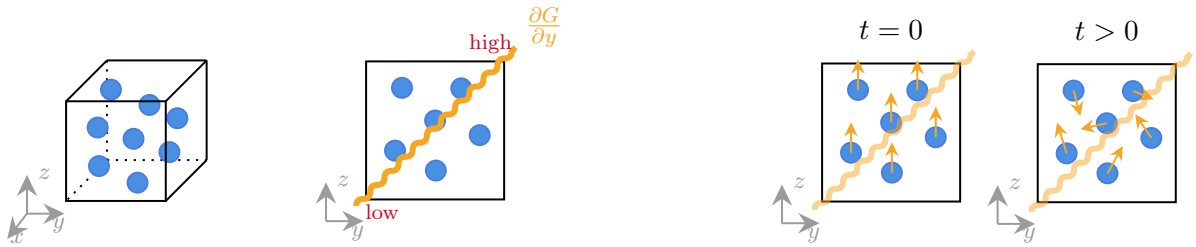

(a) **(b)**

Figure 9: *(a) Illustrates how gradients may be applied along a particular axis. (b) Illustrates how magnetic spins may evolve through time as a magnetic gradient is applied.*

4.1.2. Magnetic Gradients

Across each voxel, MRI applies magnetic gradients (low magnetic field at one side, high magnetic field at the opposite side). Depending upon how much of a magnetic field each water molecule experiences, the magnetic spin will change by different amounts. Axis-by-axis, we may apply a magnetic gradient, i.e. we apply a magnetic gradient in the x-direction, then a gradient in the y-direction, then a gradient in the z-direction; Figure 9(a) shows a gradient applied in the y-direction. As a magnetic gradient is applied, the magnetic spins will begin to change over time. Illustrated in Figure 9(b) are the magnetic spins of particles that are initially uniformly oriented, but because of the magnetic gradient are at some later time are no longer uniformly oriented.

Magnetic gradients can be parametrised with the so-called b-value. Assuming the maximum magnetic gradient is the same in each direction ($\frac{\partial G}{\partial x} = \frac{\partial G}{\partial y} = \frac{\partial G}{\partial z} \equiv G'$), the magnitude is given as

$$|G'| = \sqrt{\frac{b}{\gamma^2 \delta^2 (\Delta - \delta/3)}},$$

where γ, δ, and Δ are parameters specific to how the system is set up. Magnetic gradients are applied in pulses through time; δ and Δ are measured in units of time and respectively measure the length of gradient pulses and length before the gradient changes direction (see Figure 10).

4.1.3. Phase

The phase for an individual molecule for each axis is calculated as

$$\phi_x^j = \gamma \int_0^T G' x(t)\, \mathrm{d}t,$$

$$\phi_y^j = \gamma \int_0^T G' y(t)\, \mathrm{d}t,$$

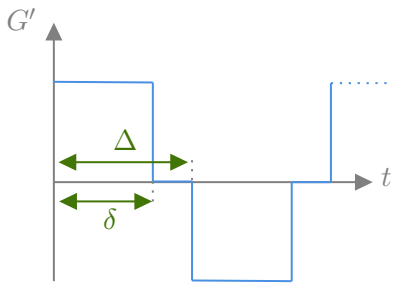

Figure 10: *Diagram illustrates how gradients are applied through time.*

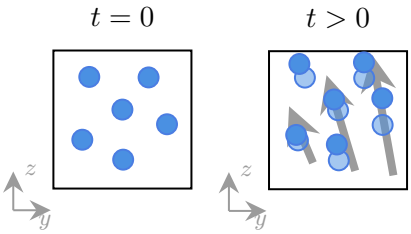

Figure 11: *Diagram illustrates how water molecules may move with the underlying velocity field; the grey arrows indicate the direction and magnitude of the velocity field.*

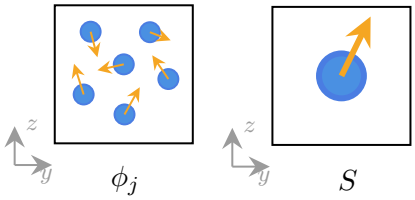

Figure 12: *Diagram illustrates how the S-value roughly corresponds to the average phase for all water molecules.*

$$\phi_z^j = \gamma \int_0^T G' z(t)\,\mathrm{d}t,$$

where $(x(t), y(t), z(t))$ gives the position of a molecule at time t, j is an index selecting each particle, and T is the final time of the measurement. We note that the phase may change through time due to both the gradient as well as position. Figure 11 illustrates how molecules may move through time and therefore may experience different magnetic gradients as their position changes.

4.1.4. *S*-value

The S-value roughly indicates the average phase in each voxel, as illustrated in Figure 12. For the phase of each molecule, ϕ_j, we calculate

$$S_x = \sum_j \exp\left(-i\phi_x^j\right),$$

$$S_y = \sum_j \exp\left(-i\phi_y^j\right),$$

$$S_z = \sum_j \exp\left(-i\phi_z^j\right),$$

where i here is the imaginary unit. The S-value is calculated simply as $S = S_x + S_y + S_z$.

4.1.5. Quantities of interest

The 'standard' MRI pictures that one would expect to see are usually a 2D slice in space (say, a rectangular slice in the x-y plane for a fixed z), for a fixed b (i.e. for a fixed choice of magnetic

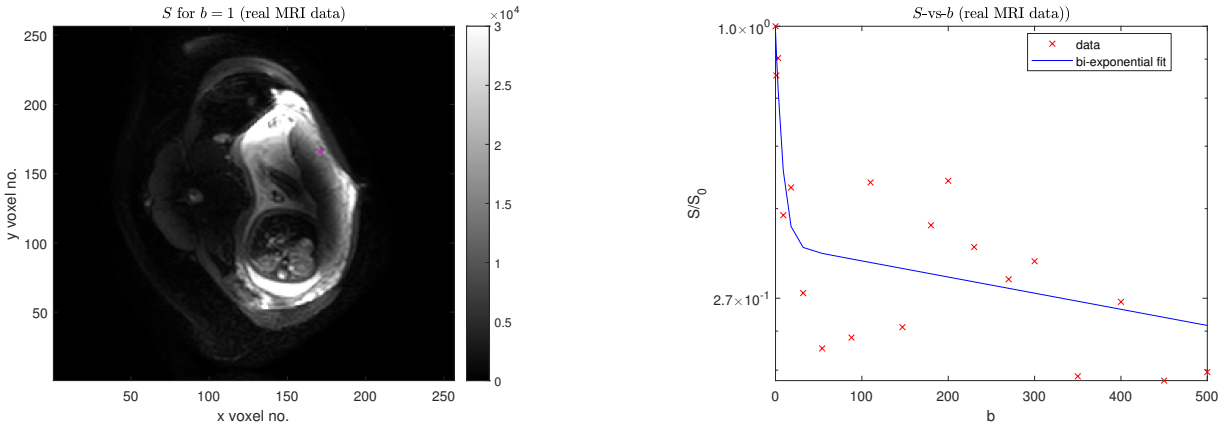

(a) **(b)**

Figure 13: *(a) An example of a 'standard' MRI image, showing a placenta and the attached fetus. Provided by private correspondence with George Hutchinson. (b) Corresponding S-vs-b plot to that selected by the magenta-coloured cross in Figure 13(a), with a bi-exponential fit of the data.*

gradient), and an appropriate colourbar scale chosen for S. An example MRI image of the placenta and surrounding area is shown in Figure 13(a) for $b = 1$. More useful quantities compared to these 'standard' pictures are in fact plots of S-vs-b for specific single voxels (ie, given (x, y, z) coordinate); the 'standard' MRI pictures allow for study of changing S-value over a single x-y slice, but it is useful to also study the relationship of quantities over other axes. For some sets of data, the relationship between S and b can be modelled by a bi-exponential fit; i.e. we want to fit to something of the form

$$S = S_0(f_{\text{IVIM}} \exp\{-bD^*\} + (1 - f_{\text{IVIM}}) \exp\{-bD\}),$$

where we fit for the parameters S_0, f_{IVIM}, D, and D^*. A full explanation of these parameters can be found at [45], but a rough list of explanations is: D describes the amount of diffusion of molecules due to random collisions between *individual* molecules; D^* describes the amount of so-called pseudodiffusion, which relates to the *collective* motion of molecules; f_{IVIM} denotes the fraction of molecules that experience the pseudodiffusion (and $(1 - f_{\text{IVIM}})$ describes the fraction of molecules that experience diffusion); S_0 is simply a scaling constant. These parameters describe intravoxel incoherent motion (IVIM), which manifests itself in the data by seeing two regions of decay in the S-vs-b plots — the two regions are separated due to $D^* \approx 10D$, helpfully allowing MRI scanners to study both phenomena. An example of an S-vs-b graph with an IVIM fit is given in Figure 13(b), for which this voxel's data corresponds to the voxel marked with a magenta cross in Figure 13(a). We note that the fit of the bi-exponential is not perfect: the fit is designed to describe molecules that are diffusing at either of the two different rates (D and D^*), for a different volume fraction (f_{IVIM}). Despite this, as well as some clear noise contamination, the data in Figure 13(b) is reasonably well approximated by the IVIM fit shown in blue, showing a faster diffusion effect between $b = 1$ and approximately $b = 20$ for the pseudodiffusion, and a slower 'true' diffusion effect for $b > 20$.

4.2. Synthetic MRI Measurements

To ultimately compare simulated velocity fields with real velocity fields, we aim to simulate the physics described in Section 4.1 and recreate what an MRI scanner may have read had the flow been physical, so that we can make direct comparison with MRI measurements.

Simulating the MRI quantities on the velocity solution presented in Section 3.1, shown in Figure 5(b), we arrive at Figure 14; note that the figure shown in this report is not the full figure, rather the full figure can be viewed online via https://phd2.blakey.family/. We note that an interesting phenomenon is shown in voxel number 101, taken from 15; notably, the fitted f_{IVIM} curve simulated data fails to describe the bouncing effect (also known as refocusing), where the descent of S against b temporarily

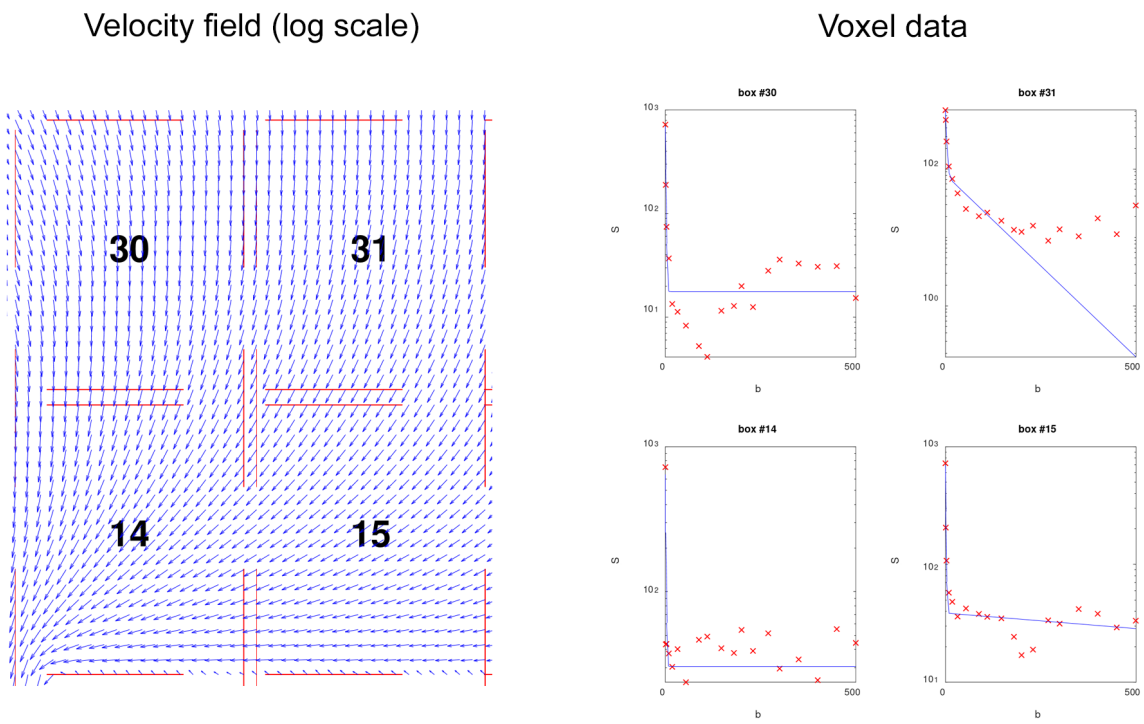

Figure 14: *(incomplete) View full-resolution image online at https://phd2.blakey.family/. This is a synthetic MRI simulation containing 256 voxels on a placentone; only 4 are shown here for ease of presentation. Please view the full-resolution image via the link. Left shows logarithmically-scaled velocity profile for a single placentone; right shows the corresponding S-vs-b plots for each indicated voxel. Voxels are assumed to be* $2.5\,\text{mm} \times 2.5\,\text{mm}$ *in size.*

ascends before descending again, which are usually found in areas of rapid flow [5]. Regardless, the f_{IVIM} fits are pretty good at describing the behaviour of the data for most voxels, and are computed as standard in the placental MRI literature.

4.3. Toward Model Validation

Earlier in the report, Figure 13(a) showed S for an MRI scan of a patient's placenta; for the same scan, we may plot the fitted value of f_{IVIM} in the x-y slice for a single b-value, giving a single number per voxel, which shown in Figure 16(a); note that we only plot f_{IVIM} for the region of interest (i.e the placenta) and set $f_{\text{IVIM}} = 0$ elsewhere. We can compare the subfigures of Figure 16, noting that Figures 16(a) and 16(b) in the top row correspond the real world data, and Figures 16(c) and 16(d) in the bottom row correspond to simulated data from our Darcy-Brinkman model. Since our generation of synthetic MRI data is performed only on a single placentone and the real MRI data is given on the entire placenta, we can't be exactly sure on how to match the voxels between the real and simulated data. Roughly, f_{IVIM} tells us what proportion of the fluid is moving quickly, so using Figure 16(a) we may be able to cross-reference areas of high f_{IVIM} on the real MRI data with areas we know to have high velocity in the simulated velocity field. The relatively high concentration of f_{IVIM} of the real data, located on the right side of Figure 16(a), suggests that this could be flow entering the IVS from a spiral artery, with the voxel marked with a black cross located somewhere in the IVS close to high velocity flow. We pick voxel 69 from Figure 14, which lies close to the centreline above the spiral artery in our placentone flow simulation, to make comparison with the voxel indicated with a black cross in Figure 16(a). Recalling that the real MRI data in Figure 16(b) may contain noise, this figure and the simulated MRI data in Figure 16(d) appear to have a reasonably good correspondence, after some scaling: certainly, the bi-exponential fit have the same general behaviour with the pseudodiffusion effect visible for roughly $b < 50$, and the regular diffusion effect visible for $b > 50$.

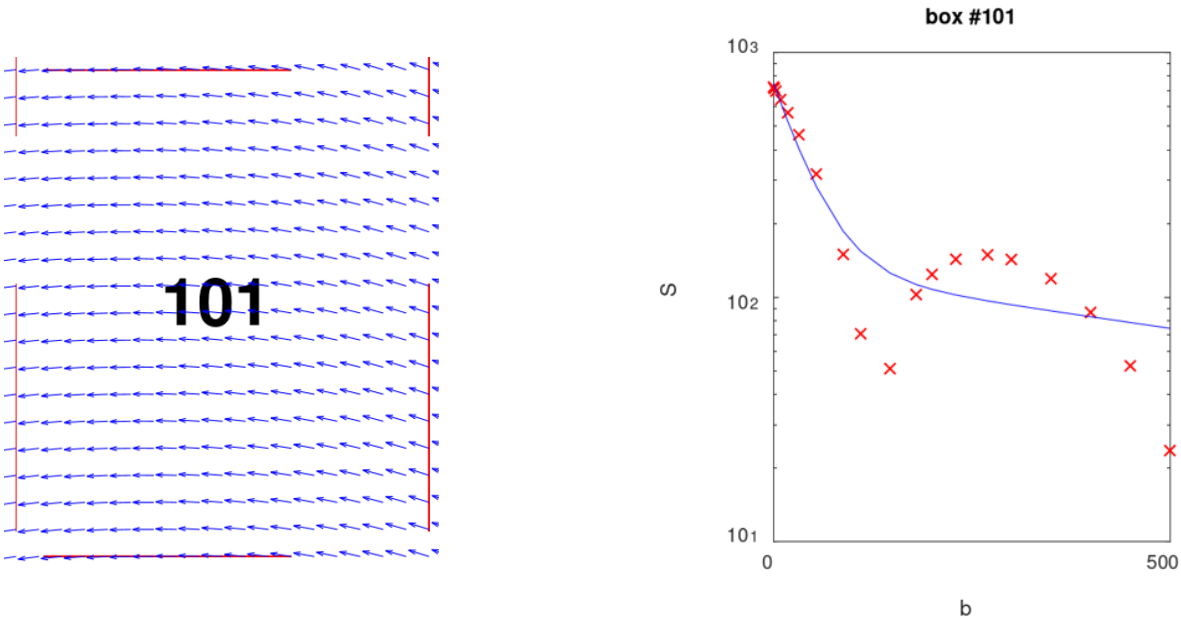

(a) (b)

Figure 15: *Zoomed-in images of Figure 14. (a) Logarithmically-scaled velocity profile for voxel number 101. (b) The corresponding S-vs-b and IVIM fit plot for voxel number 101.*

5. Model Development

5.1. Septal Veins

In Section 3.2 we modelled a 2D slice of a placenta containing 6 placentones, each with 2 veins and 1 artery, as well as 2 corner veins that are located on the chorionic plate. In this section we investigate the influence of septal veins on blood flow.

Figure 17(a) shows the existence of septal veins, for which there are thought to be 5–6 such veins in the entire placenta. Figure 17(b) shows that in a perfusion experiment that flow does pass through septa. We choose to add 4 septal veins to our 2D placental slice, mostly reusing the existing placenta domain introduced in Section 3.2. We add these 4 veins on 4 different septa, varying the height and side on which they are located on. Figure 18(a) shows the described domain.

We again run the simulations as undertaken in Section 3.2, where we have chosen the boundary conditions such that there is Poiseuille parablolic flow perpendicular to the inlets as given in Equation (8), zero outward flux on all outlets ($\mathbf{g_N} = \mathbf{0}$), and no slip elsewhere ($\mathbf{g_D} = \mathbf{0}$). We employ a mesh with refinement near inlets and outlets, ultimately giving 1,146,246 elements. Polynomial degree 2 is chosen in the velocity components and polynomial degree 1 in the pressure component. The corresponding mesh is shown in Figure 18(b).

Comparing Figures 7(b) and 19, we notice a few differences. Firstly, the simulation without septal veins is symmetric (as expected), whereas the simulation with septal veins is asymmetric, most likely due to the choice of the locations of the additional veins. Secondly, we notice that the simulation with septal veins has less slow-moving fluid; there is less blue in the simulation with septal veins. Thirdly, there appears to be more movement between placentones in the sub-chorionic space (SCS), which lies above the septal walls, when septal veins are present.

These results show that septal veins do have an impact on blood flow, in particular showing that their inclusion in the simulations produces less slow-moving fluid, and therefore may be important in the transport of nutrients through the placenta.

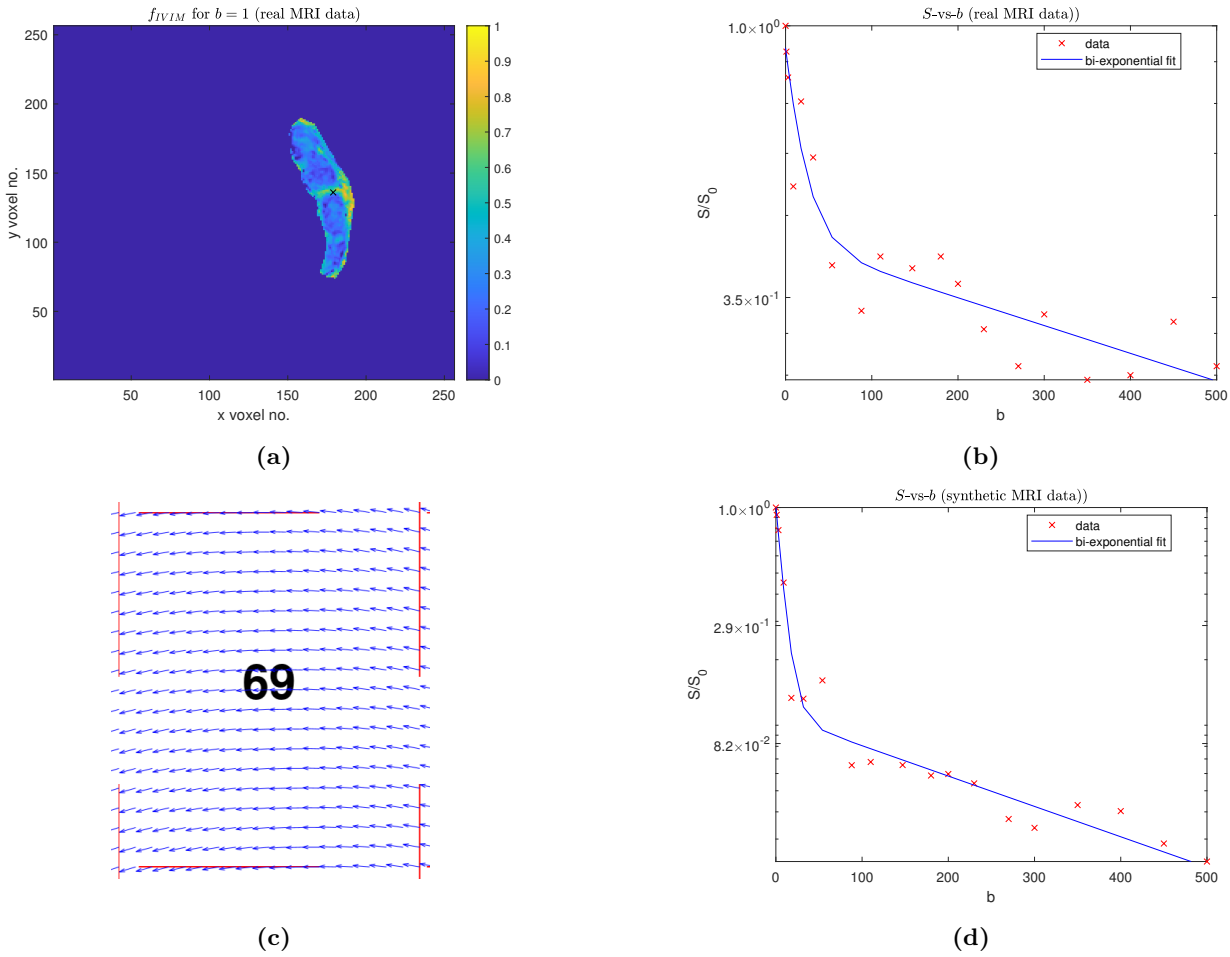

Figure 16: *Comparison of real MRI data with the simulated MRI data from our flow model. (a) The fitted f_{IVIM} from real MRI data over the entire placental area. (b) The corresponding S-vs-b and IVIM fit plot for the voxel marked with a black cross in (a). (c) Logarithmically-scaled velocity profile for voxel number 69 on the simulated velocity field, from Figure 15(a). (d) The corresponding S-vs-b and IVIM fit plot for (c).*

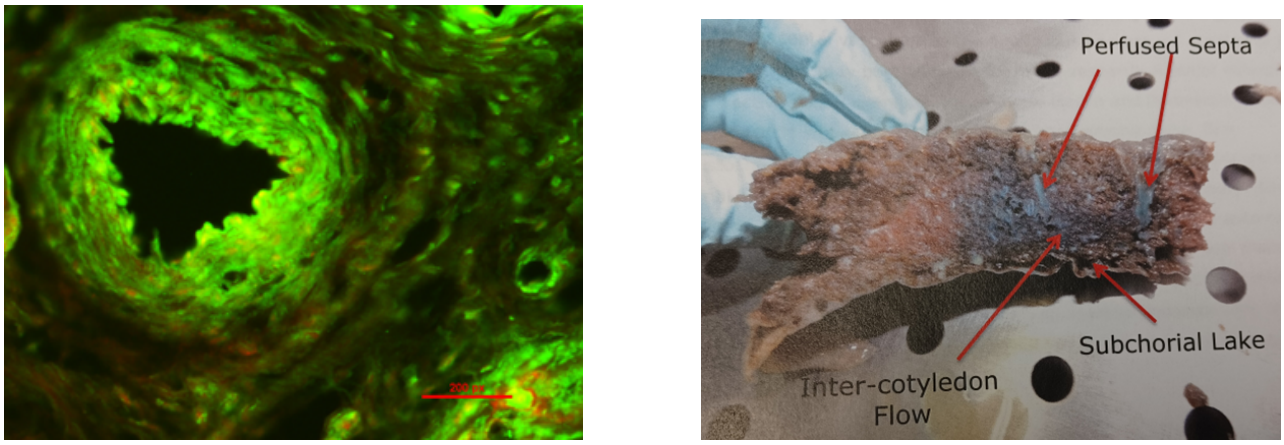

Figure 17: *Images provided by private correspondence with Lopa Leach. (a) Fluorescent staining of a visible opening on a septal wall. (b) Septa between placentones (or equivalently cotyledons) are perfused with blood; blue ink injected into one placentone is shown to have flowed into veins of septa and toward the marginal sinus.*

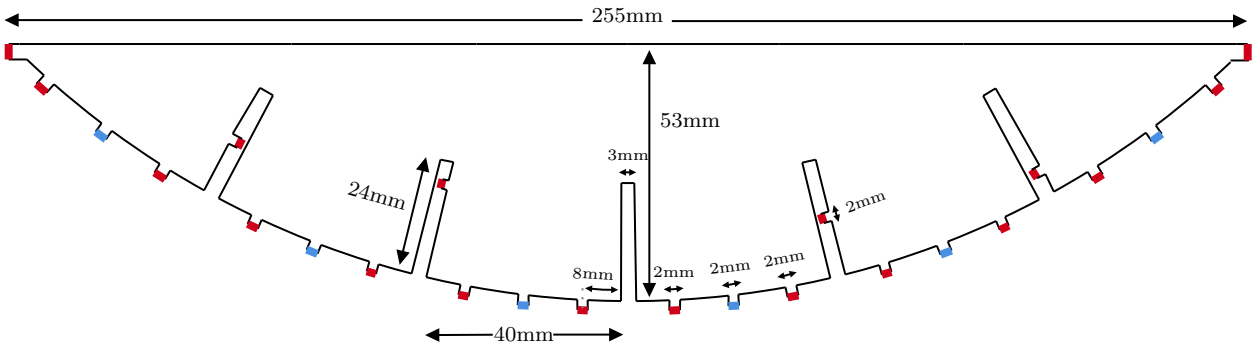

(a)

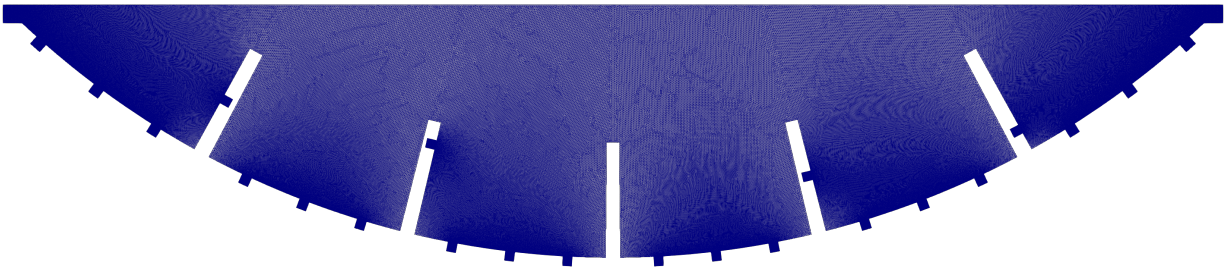

(b)

Figure 18: *(a) Diagram illustrates a simple 2D geometry for a slice of the whole placenta, consisting of 6 adjacent placentones, with an additional 4 veins located on the septa. (b) Mesh used for simulation described in Section 5.1.*

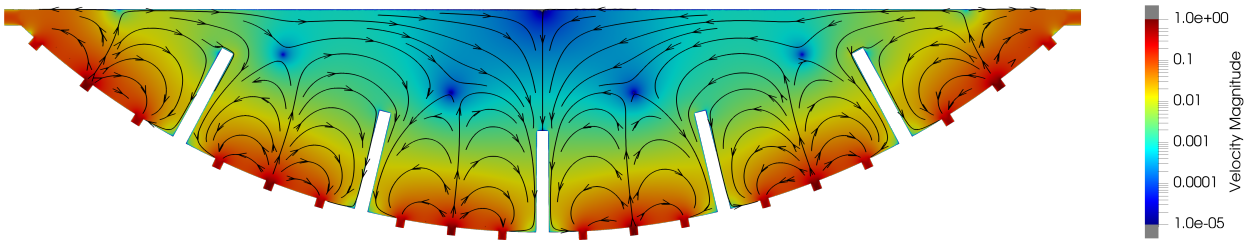

Figure 7(b): *(repeated) Plot showing logarithmic velocity magnitude in colour (blue is slow, red is fast) with black streamlines and arrows for the placentone simulation described in Section 3.2.*

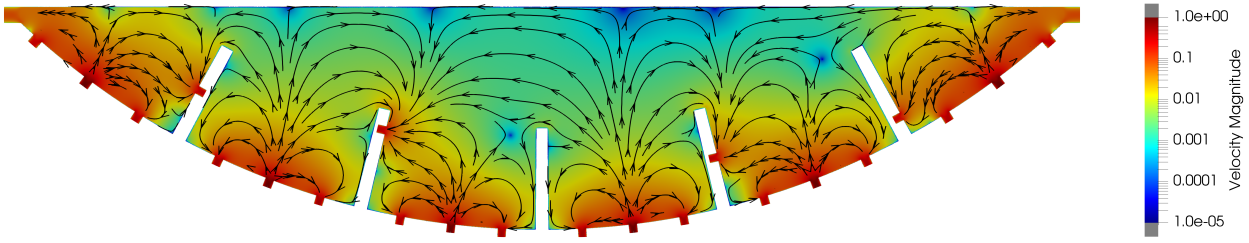

Figure 19: *Plot showing logarithmic velocity magnitude in colour (blue is slow, red is fast) with black streamlines and arrows for the placentone simulation described in Section 5.1.*

5.2. Nutrient Transport

Reaction-advection-diffusion equations are commonly used for modelling the transport of physical quantities that experience a combination of reactive, advective, and diffusive processes. This equation can be utilised in nutrient transport by forming a one-way coupling from the velocity field equations to the reaction-advection-diffusion equations ([46, 47]); that is to say, in this context, we solve the Darcy-Brinkman flow field, from which the computed flow field will form the convective velocity in the first-order term of the proposed reaction-advection-diffusion model.

We focus on modelling transport of nutrients from maternal blood to fetal blood. We once again split the domain boundary, $\partial\Omega$, into two disjoint sets, Γ_D^{RAD} and Γ_N^{RAD}, respectively corresponding to the Dirichlet and Neumann conditions of the reaction-advection-diffusion problem; we again have the restrictions that $\Gamma_D^{\text{RAD}} \neq \emptyset$ and $\Gamma_N := \partial\Omega \setminus \Gamma_D^{\text{RAD}}$. Note that Γ_D^{RAD} and Γ_N^{RAD} which define the Dirichlet and Neumann boundaries, respectively, for this problem may in general be different to those from regions chosen in our Darcy-Brinkman equations in Equation (2). The dimensional reaction-advection-diffusion equations are given by: find c such that

$$\frac{\partial c}{\partial t} - D\nabla^2 c + \boldsymbol{\nabla} \cdot (\mathbf{u}c) + Rc = f^{\text{RAD}} \text{ in } \Omega, \tag{9a}$$

$$c = g_D^{\text{RAD}} \text{ on } \Gamma_D^{\text{RAD}}, \tag{9b}$$

$$\nabla c \cdot \mathbf{n} = g_N^{\text{RAD}} \text{ on } \Gamma_N^{\text{RAD}}, \tag{9c}$$

where f^{RAD}, g_D^{RAD}, and g_N^{RAD} are functions of the spatial coordinates, t is time, D is a scalar diffusion coefficient, $\mathbf{u}(\mathbf{x})$ is a prescribed convective transport velocity on Ω obtained from the approximation to Equation (3), and R is a scalar reaction coefficient.

We nondimensionalise this problem with scalings: $c \to Cc$, $\mathbf{x} \to L\mathbf{x}$, $\mathbf{u} \to U\mathbf{u}$, $t \to \frac{L}{U}t$, $f^{\text{RAD}} \to \frac{CU}{L} f^{\text{RAD}}$; where L is the same length-scale chosen for the Darcy-Brinkman model, U is the same velocity-scale chosen for the Darcy-Brinkman model, and C is the scaling of the concentration we are simulating.

Substituting these variables gives us our nondimensional reaction-advection-diffusion equations: find c such that

$$\frac{\partial c}{\partial t} - \frac{1}{Pe}\nabla^2 c + \boldsymbol{\nabla}\cdot(\mathbf{u}c) + Dm\, c = f^{\mathrm{RAD}} \text{ in } \Omega, \tag{10a}$$

$$c = g_D^{\mathrm{RAD}} \text{ on } \Gamma_D^{\mathrm{RAD}}, \tag{10b}$$

$$\nabla c\cdot\mathbf{n} = g_N^{\mathrm{RAD}} \text{ on } \Gamma_N^{\mathrm{RAD}}, \tag{10c}$$

where $Pe := \frac{LU}{D}$ is the Péclet number that describes ratio of advection-to-diffusion, and $Dm := \frac{RL}{U}$ is the Damköhler number that describes ratio of reaction-to-advection.

For the discretisation of our nondimensional reaction-advection-diffusion equations in Equation (10), we first take a simple finite-difference for the $\frac{\partial c}{\partial t}$ term. We introduce time levels

$$0 = t^0 < t^1 < ... < t^N,$$

where $N \in \mathbb{N}$, and take a backward (implicit) Euler method by setting

$$\frac{\partial c^{n+1}}{\partial t} \to \frac{c^{n+1} - c^n}{\Delta t},$$

where we are looking to solve for c at the $(n+1)$st step, $n \in \mathbb{N}$, and exponents here denote time step values; that is, c^n represents $c(\mathbf{x})$ at time-step number n, and c^{n+1} represents $c(\mathbf{x})$ at time-step number $n+1$. The time-stepping here is uniform (i.e. $\Delta t = t^{n+1} - t^n$ is constant for all n).

Similarly to Section 2.1, we introduce the finite element space

$$\mathbf{W}_h := \{w \in L^2(\Omega) : w|_\kappa \in \mathcal{P}_r(\kappa), \kappa \in \mathcal{T}_h\}. \tag{11}$$

With minor modification to [26] to account for the $\frac{\partial c}{\partial t}$ term, we can give our DGFEM discretisation of the nondimensional reaction-advection-diffusion equations: find $c_h^{n+1} \in W_h$ such that

$$\begin{aligned}
&\int_\Omega (c_h^{n+1} d_h + \frac{1}{Pe}\nabla c_h^{n+1}\cdot\nabla d_h + (\nabla\cdot\mathbf{u})c_h^{n+1} d_h + (\nabla c_h^{n+1}\cdot\mathbf{u})d_h + Dm\, c_h^{n+1} d_h)\,\mathrm{d}\mathbf{x} \\
&\quad + \int_{F_h^I \cup F_h^D} (-\{\!\{\frac{1}{Pe}\nabla c_h^{n+1}\}\!\}\cdot[\![d_h]\!] - \{\!\{\frac{1}{Pe}\nabla d_h\}\!\}\cdot[\![c_h^{n+1}]\!] + \sigma^{\mathrm{RAD}}[\![c_h^{n+1}]\!]\cdot[\![d_h]\!])\,\mathrm{d}\mathbf{x} \\
&- \sum_{\kappa\in T_h}\int_{\partial_-\kappa\setminus\partial\Omega} \mathbf{u}\cdot\mathbf{n}_\kappa (c_h^{n+1,+} - c_h^{n+1,-}) d_h^+\,\mathrm{d}s - \sum_{\kappa\in T_h}\int_{\partial_-\kappa\cap\Gamma_D^{\mathrm{RAD}}} \mathbf{u}\cdot\mathbf{n}_\kappa c_h^{n+1,+} d_h^+\,\mathrm{d}s \\
&\qquad = \int_\Omega f^{\mathrm{RAD}} d_h\,\mathrm{d}\mathbf{x} + \int_{\Gamma_D^{\mathrm{RAD}}} g_D^{\mathrm{RAD}}(\sigma^{\mathrm{RAD}} d_h - \nabla d_h)\,\mathrm{d}s + \int_{\Gamma_N^{\mathrm{RAD}}} g_N^{\mathrm{RAD}} d_h\,\mathrm{d}s \\
&\qquad\qquad - \sum_{\kappa\in T_h}\int_{\partial_-\kappa\cap\Gamma_D^{\mathrm{RAD}}} \mathbf{u}\cdot\mathbf{n} g_D^{\mathrm{RAD}} d_h^+\,\mathrm{d}s
\end{aligned} \tag{12}$$

for all $d_h \in W_h$, for each given c_h^n for $n \in [0, N]$ (N is total number of time steps), where $\sigma^{\mathrm{RAD}} = 10\frac{r^2}{h}$ is the DGFEM symmetric interior penalty parameter for total polynomial degrees r on each element, $\kappa \in \mathcal{T}_h$, $\partial_-\kappa$ denotes the region of outflow flux from an element, $\kappa \in \mathcal{T}_h$, and c^-, d^- respectively denote the exterior traces of c and d, and c^+, d^+ respectively denote the interior traces of c and d. Note throughout this discretisation that all scripts with 'RAD' denote that these are different to their equivalents chosen for the Darcy-Brinkman problem in Section 2.2, and are specific to the current reaction-advection-diffusion problem.

We run a simulation on the whole placenta domain, sketched in Figure 18(a), where we first solve our Darcy-Brinkman equations from Equation (3) for a steady-state velocity field, which is then one-way coupled through $\mathbf{u}$ to the reaction-advection-diffusion equation in Equation (10). We choose parameters values specific to oxygen transport, but the details so far can be applied to modelling of other nutrients.

For oxygen, we set $f^{\mathrm{RAD}} = 0$ for no external forcing, $L = 4 \times 10^{-2}$ [11], $k = 1 \times 10^{-8}$ [9], $U = 1 \times 10^{-1}$ [12], $D = 1.667 \times 10^{-9}$ [11], $R = 1.667 \times 10^{-2}$ [11]; these choices yield $Pe = 2.400 \times 10^6$

and $Dm = 6.667 \times 10^{-3}$. We select a mesh that has been h-adapted 1 time according to the velocity solution (refining the elements with indicators on the velocity solution in the top 30% among all error indicators), which is shown in Figure 20(a). We select polynomial degree 2 in the velocity components, 1 in the pressure space, and 1 in the space for the concentration of nutrients, c. We set the boundary conditions as chosen in Section 3.2 for the velocity problem, and for the concentration problem we set $g_D^{\mathrm{RAD}} = 1$ on inlets and $g_D^{\mathrm{RAD}} = 0$ on outlets. We set $\Delta t = 1$ and run until $t = T := 1000$. We also set an initial condition at time $t = 0$ of $c_0 = 0$ everywhere except the inlets. Still images of the nutrient transport simulation at nondimensional times $t = 1$, $t = 30$, $t = 120$, and $t = 1000$ are shown in Figures 20(b)–20(e); note that due to the choice of scalings that these respectively correspond to dimensional times 0.2 s, 12 s, 48 s, and 400 s.

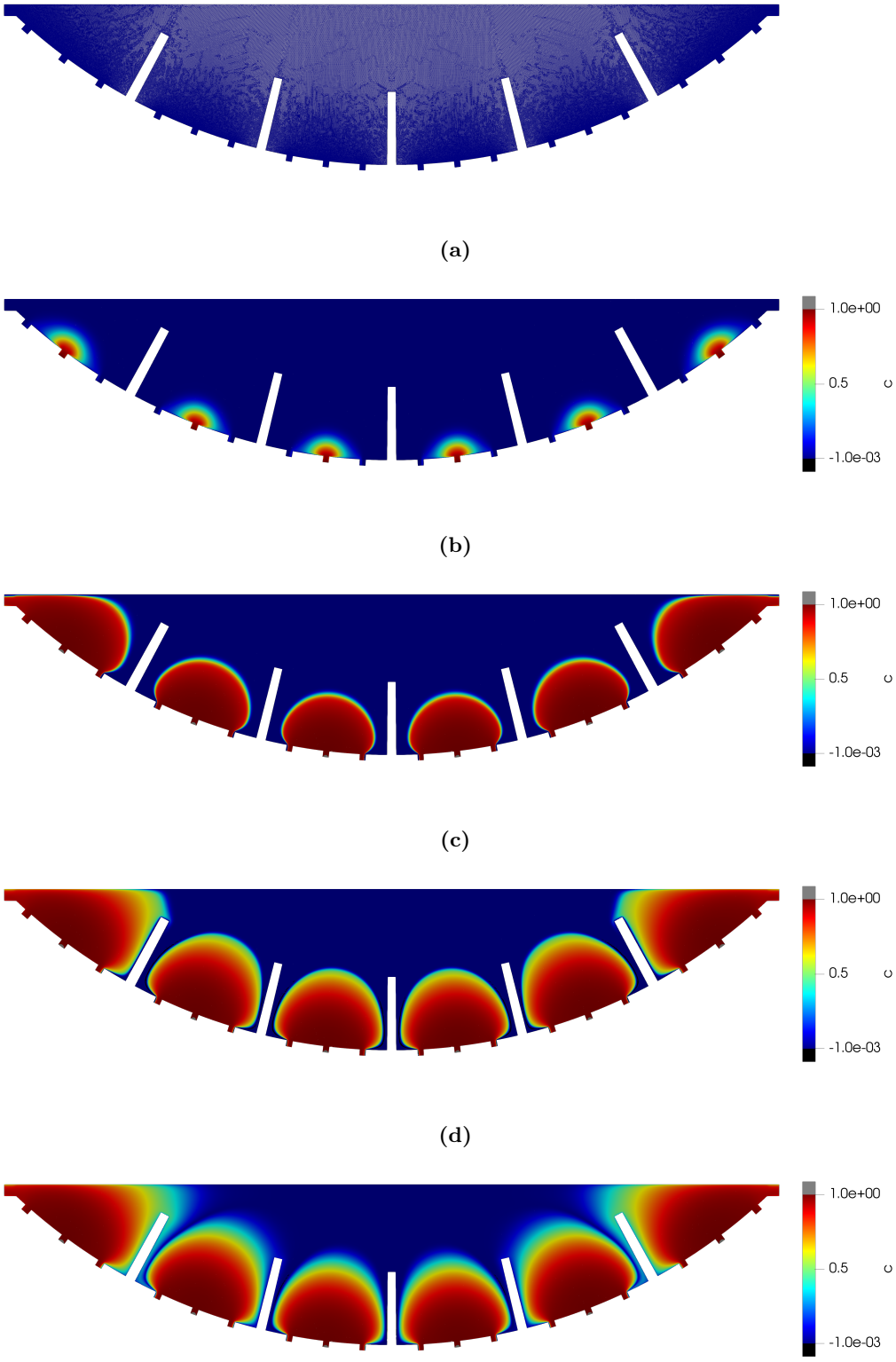

Figure 20: *(a) Mesh of the oxygen transport simulation described in Section 5.2. (b–e) Still images of concentration of oxygen transported by maternal blood flow for nondimensional times (b) $t = 1$, (c) $t = 30$, (d) $t = 120$, (e) $t = 1000$; please see https://phd2.blakey.family/ for full animation.*

Figure 20(b) shows the oxygen concentration shortly after the simulation has begun; we see that the concentration is spreading radially from the inlet location. We note that this is the point in the simulation where the concentration is moving quickest, due to the high velocity of blood near the inlet. Figure 20(c) shows the concentration of oxygen after it has reached the outlets immediately neighbouring the inlets; the oxygen concentration has already reached the corner outlets by this time. Figure 20(d) shows the oxygen concentration as some of the oxygen begins to be transported over the walls from the outer-most placentones to the next placentones, showing that oxygen entering in one placentone may exit through another. Figure 20(e) shows the oxygen concentration at the final time of our simulation, and after the oxygen concentration from outer-most placentones has been transported to neighbouring placentones' outlets. The full animation is available at https://phd2.blakey.family/.

5.3. Variable Permeability

We model the IVS in which maternal blood flows as a porous medium, but throughout Section 3 we have so far neglected the fact that the villous tree may not necessarily span the entire IVS. For instance, it has been reported by several authors that central cavity (the area that is located directly above the spiral artery) is thought to contain no villous tree whatsoever [9, 12]. In the simulations of Lecarpentier et al. [9], they make an elliptical area above the central cavity in which they simulate the Navier-Stokes equations, and elsewhere simulate Darcy-Brinkman, in an attempt to properly capture the dynamics of the central cavity. For simplicity, in this section we will solve Darcy-Brinkman everywhere, but vary the permeability, k, in different regions.

We run the varying-permeability simulation with very similar parameters to those chosen in Section 3.1: $L = 0.04$, and $k = 10^{-8}$ in most places, with $k = 10^{-7}$ in the regions around the inlets and outlets; we make these regions elliptical around the inlet [9], and circular around the outlets. Boundary conditions are set identically to those in Section 3.1: Poiseuille parabolic inflow on the inlet given in Equation (7), zero outward flux ($\mathbf{g_N} = \mathbf{0}$), and no slip elsewhere ($\mathbf{g_D} = \mathbf{0}$). And similarly, the polynomial degrees are chosen as 2 in the velocity components and 1 in the pressure space. However, a notable modification to the simulations in Section 3.1 is that we use an h-adapted mesh; we found by using the same mesh, we found many spurious oscillations in the solution. By performing 2 steps of h-adaptivity, where at each step we refined elements that had error indicator values in the top 30% among all error indicators, we get the mesh shown in Figure 21(a), which is more refined primarily on the interface between the two choices of permeability. Figure 21(b) shows the resulting solution, where we've solved Stokes flow in the inlet and outlet pipes, and Darcy-Brinkman elsewhere.

Clearly there is more work to be completed here in terms of varying the permeability of the porous medium, in particular on the scale of the entire placenta. Clark et al. [8] suggest that there are 60–100 individual trees in the placenta — roughly there is one tree per placentone. It would be interesting to consider modelling the dynamics at the 'trunks' of these trees (where there may be larger solid branches) either by varying the permeability, or by resolving trees exactly in this region and adopting a free-flow model such as Stokes or Navier-Stokes.

6. Conclusions and Future Research Plan

In this report, we have given an overview of the placental modelling literature, and have a flow model of maternal blood through the villous tree in the IVS of the placenta. Some authors in the literature have considered simulations that resolve the villous tree exactly [9], but these can be expensive due to the need for a high-resolution mesh and need for a free-flow model such as Navier-Stokes. We instead opted for a porous medium description of the villous tree, for which we utilised a Darcy-Brinkman fluid flow model. However, as reported by Burton et al. [12], the Reynolds number of flow in the spiral artery is likely 20–80, which suggests that a better fluid flow model in the limited regions of high flow rate may be more appropriate than our current models of Darcy-Brinkman and Stokes. Furthermore, our model neglects the natural pulsatility of blood flow [48], and also the widening of the spiral artery as it enters the IVS [12, 13], which are likely important features of blood flow in the placenta.

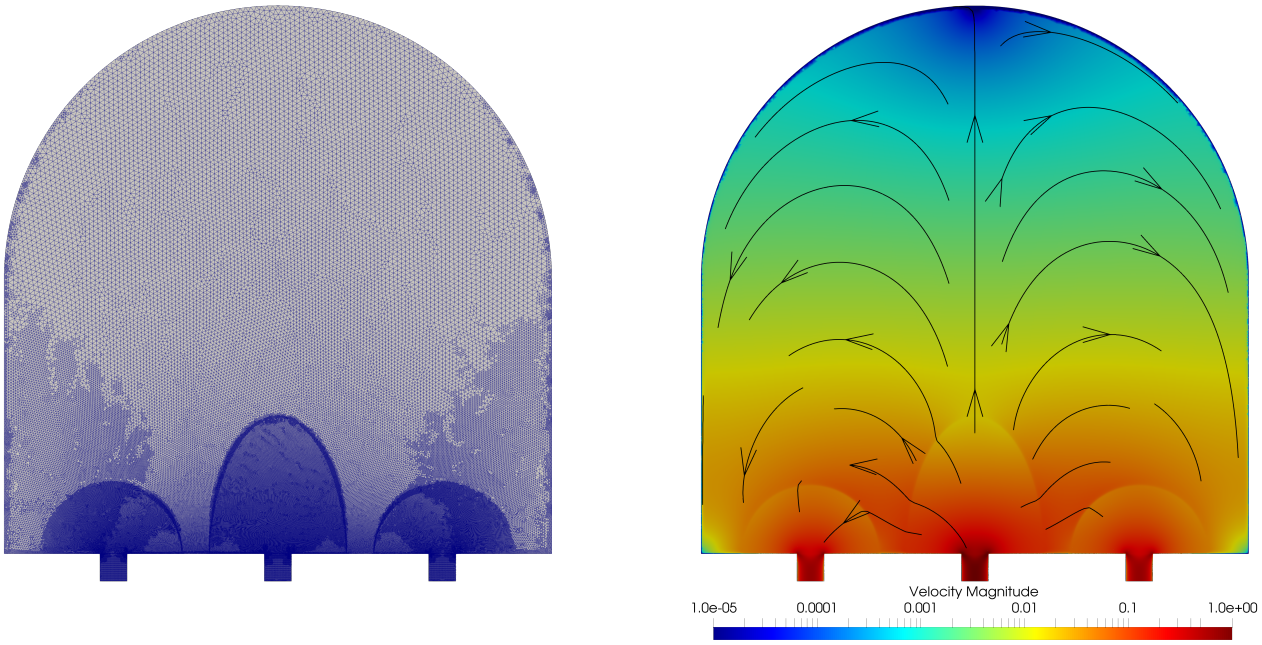

(a) **(b)**

Figure 21: *(a) Mesh for simulation described in Section 5.3 after 3 h-adaptive refinement steps. (b) Plot showing logarithmic velocity magnitude in colour (blow is flow, red is fast) with black streamlines and arrows for the variable permeability simulation described in Section 5.3.*

We considered maternal blood flow in representative 2D placentone and 2D whole placenta domains, for which the results agreed with work completed by Chernyavsky, Jensen, and Leach [11], and Lecarpentier et al. [9]. However, unlike the work in [11], we did not consider the effect of moving arteries and veins within these idealised domains; from the work by Dellschaft et al. [5], they found that oxygen was delivered relatively uniformly across the placenta in vivo, and they suggested that this could be due to the measured slow maternal blood flow rates. In diseased cases such as pre-eclampsia, the maternal blood flow rates can be much higher [5, 12]. It would therefore be interesting to form a range of numerical experiments that vary the inlet and outlet conditions and locations to see what effect this has on the uniformity of nutrient delivery.

To pave the way for validation of our model, we introduced a new technique for synthetically generating MRI data from a simulated velocity field, allowing for direct comparison with the measurements MRI scanners make. We note that this technique is not specific to placental flows. We showed that certain features were present in both the real MRI data and the synthetically generated MRI data. An issue we encountered was how to match the voxel data from the idealised simulated domains to the real data; we did this by matching areas of high flow in, but a better matching process is likely needed, especially for areas away from the spiral artery. A natural extension to the work presented would be to also generate MRI data from the whole placenta domain and compare again to real MRI data. A potential paper may follow containing full details, in collaboration with George Hutchinson and Penny Gowland. Further validation of our model may be performed with ex-vivo perfusion experiments by another one of our collaborators, Lopa Leach.

We separately considered 3 different modifications to our model. Firstly, we incorporated additional septal veins, which showed that their inclusion gave less slow-moving blood, and therefore may be important in the transport of nutrients through the placenta. Secondly, we coupled a nutrient transport model to the blood flow simulations which show that nutrients could be transported between neighbouring placentones. Thirdly, we varied the permeability throughout the single placentone domain to more accurately describe flow in the central cavity; a natural extension of this work would be to vary the permeability in the whole placenta domain, potentially capturing the effects of larger villous tree structures near the chorionic plate, or varying the permeability due to both space and velocity

similarly to Erian, Corrsin, and Davis [10].

In this report, the placenta has been modelled only as a two-dimensional, rigid object with steady-state flow; however, the placenta itself is very much a three-dimensional, time-dependent object. Huge computational challenges arise can arise in this regime, so careful consideration will have to be given to which features are most important to model. Chernyavsky, Jensen, and Leach derive an analytic expression for a Darcy's Law in a hemisphere [11], but this relies on some undesirable assumptions such as the outlets being symmetrical about the inlet, and that the centres of inlets and outlets must lie on a straight line; with the numerical methods developed here, although more computationally expensive than analytic expressions, we do not have this limitation. We found the nutrient transport simulation particularly challenging to run, despite being in 2D: we found that without a very high resolution solution for the velocity solution, we would later find severe oscillations in the transport solution as time progressed; adaptivity may be crucial in making this computationally easier, and ultimately needs more investigation.

Future work over the coming months will concentrate on modelling the effects of the 'utero-placental pump' phenomena reported by Dellschaft et al. [5], which will fully utilise the expertise in the supervisory team for accurately modelling the phenomena, implementation of the arising FSI moving-boundary problems, and ensuring that this is done with computational efficiency. Additionally, the whole placenta geometry in this report neglected the muscular walls of the marginal sinus and may be an important feature to model, and could potentially utilise some of the work with moving boundaries.

To give a summary of a summary, this year I have:

- Got a good grasp of the existing progress in placental modelling, including important gaps in the literature
- Have completed first steps to a biophysical model of flow and nutrient transport, with several ideas on how to improve the model, including:
  - Varying the permeability and/or model throughout the domain
  - Moving boundary simulations, to capture placental contractions
  - Limited 3D simulations
- A potential paper in coming months with George Hutchinson on synthetic MRI data generation from simulated velocity fields

References

[1] Gareth A. Nye et al. "Human placental oxygenation in late gestation: experimental and theoretical approaches". In: *The Journal of Physiology* 596.23 (2018). DOI: https://doi.org/10.1113/JP275633.

[2] Efthymios Maneas et al. "Photoacoustic imaging of the human placental vasculature". In: *Journal of Biophotonics* 13 (4 2020). DOI: https://doi.org/10.1002/jbio.201900167.

[3] Oliver E Jensen and Igor L Chernyavsky. "Blood Flow and Transport in the Human Placenta". In: *Annual review of fluid mechanics* 51.1 (2019), pp. 25–47. DOI: https://doi.org/10.1146/annurev-fluid-010518-040219.

[4] A. S. Serov et al. "The role of morphology in mathematical models of placental gas exchange". In: *Journal of Applied Physiology* 120.1 (2016). DOI: https://doi.org/10.1152/japplphysiol.00543.2015.

[5] Neele S Dellschaft et al. "The haemodynamics of the human placenta in utero". In: *PLOS Biology* 18.5 (2020), e3000676. DOI: http://dx.doi.org/10.1371/journal.pbio.3000676.

[6] Romina Plitman Mayo et al. "Three-dimensional modeling of human placental terminal villi". In: *Placenta* 43 (2016). DOI: https://doi.org/10.1016/j.placenta.2016.05.001.

[7] Yoko Kato, Michelle L. Oyen, and Graham J. Burton. "Villous Tree Model with Active Contractions for Estimating Blood Flow Conditions in the Human Placenta". In: *The Open Biomedical Engineering Journal* 11.1 (2017). DOI: https://doi.org/10.2174/1874120701711010036.

[8] A. R. Clark et al. "Multiscale modelling of the feto-placental vasculature". In: *Interface Focus* 5.2 (2015). DOI: https://doi.org/10.1098/rsfs.2014.0078.

[9] E. Lecarpentier et al. "Computational Fluid Dynamic Simulations of Maternal Circulation: Wall Shear Stress in the Human Placenta and Its Biological Implications". In: *PLOS ONE* 11.1 (2016), pp. 1–18. DOI: https://doi.org/10.1371/journal.pone.0147262.

[10] F.F. Erian, S. Corrsin, and S.H. Davis. "Maternal, placental blood flow: A model with velocity-dependent permeability". In: *Journal of Biomechanics* 10.11 (1977), pp. 807–814. DOI: https://doi.org/10.1016/0021-9290(77)90095-1.

[11] I. L. Chernyavsky, O. E. Jensen, and L. Leach. "A mathematical model of intervillous blood flow in the human placentone". In: *Placenta* 31.1 (2010), pp. 44–52. DOI: https://doi.org/10.1016/j.placenta.2009.11.003.

[12] Graham J. Burton et al. "Rheological and Physiological Consequences of Conversion of the Maternal Spiral Arteries for Uteroplacental Blood Flow during Human Pregnancy". In: *Placenta* 30.6 (2009). DOI: https://doi.org/10.1016/j.placenta.2009.02.009.

[13] Christian J. Roth et al. "Dynamic modeling of uteroplacental blood flow in IUGR indicates vortices and elevated pressure in the intervillous space-a pilot study". In: *Scientific Reports* 7.August 2016 (2017). DOI: https://doi.org/10.1038/srep40771.

[14] Rojan Saghian et al. "Association of Placental Jets and Mega-Jets with Reduced Villous Density". In: *Journal of Biomechanical Engineering* 139.5 (2017). DOI: https://doi.org/10.1115/1.4036145.

[15] Igor L. Chernyavsky et al. "Transport in the placenta: homogenizing haemodynamics in a disordered medium". In: *Philosophical Transactions of the Royal Society A: Mathematical, Physical and Engineering Sciences* 369.1954 (2011), pp. 4162–4182. DOI: https://doi.org/10.1098/rsta.2011.0170.

[16] Hannah J. Pybus et al. "Reduced biomechanical models for precision-cut lung-slice stretching experiments". In: *Journal of Mathematical Biology* 82.35 (2021). DOI: https://doi.org/10.1007/s00285-021-01578-2.

[17] Barbara J. Breen et al. "Quantifying parenchymal tethering in a finite element simulation of a human lung slice under bronchoconstriction". In: *Respiratory Physiology & Neurobiology* 183.2 (2012). DOI: https://doi.org/10.1016/j.resp.2012.06.014.

[18] Anne E. Farley, Charles H. Graham, and Graeme N. Smith. "Contractile properties of human placental anchoring villi". In: *American Journal of Physiology-Regulatory, Integrative and Comparative Physiology* 287.3 (2004). DOI: https://doi.org/10.1152/ajpregu.00222.2004.

[19] Kaori Togashi et al. "Sustained uterine contractions: A cause of hypointense myometrial bulging". In: *Radiology* 187.3 (1993). DOI: https://doi.org/10.1148/radiology.187.3.8497617.

[20] J. Collis et al. "Effective equations governing an active poroelastic medium". In: *Proceedings of the Royal Society A: Mathematical, Physical and Engineering Sciences* 473.2198 (2017), p. 20160755. DOI: https://doi.org/10.1098/rspa.2016.0755.

[21] Wei-Kang Sun, Lu-Wen Zhang, and K.M. Liew. "A smoothed particle hydrodynamics-peridynamics coupling strategy for modeling fluid-structure interaction problems". In: *Computer methods in applied mathematics and engineering* 371 (2020). DOI: https://doi.org/10.1016/j.cma.2020.113298.

[22] Andrey Ricardo Da Silva, Gary P Scavone, and Maarten Van Walstijn. "Numerical simulations of fluid-structure interactions in single-reed mouthpieces". In: *The Journal of the Acoustical Society of America* 122.3 (2007), pp. 1798–1809. DOI: https://doi.org/10.1121/1.2759166.

[23] Gergely Szabó, József Györgyi, and Gergely Kristóf. "Three-dimensional FSI Simulation by Using a Novel Hybrid Scaling – Application to the Tacoma Narrows Bridge". In: *Periodica Polytechnica Civil Engineering* 64.4 (2020), pp. 975–988. DOI: https://doi.org/10.3311/PPci.15586.

[24] Luca Formaggia, Alfio Quarteroni, and Allesandro Veneziani. *Cardiovascular Mathematics: Modeling and simulation of the circulatory system*. MS&A. Springer Science & Business Media, 2010. DOI: https://doi.org/10.1007/978-88-470-1152-6.

[25] Gene Hou, Jin Wang, and Anita Layton. "Numerical Methods for Fluid-Structure Interaction — A Review". In: *Communications in Computational Physics* 12.2 (2012), pp. 337–377. DOI: https://doi.org/10.4208/cicp.291210.290411s.

[26] Andrea Cangiani et al. *hp-version discontinuous Galerkin methods on polygonal and polyhedral meshes*. Springer Briefs in Mathematics. https://ebookcentral.proquest.com/lib/nottingham/detail.action?docID=5163236. Springer, 2017. ISBN: 9783319676739.

[27] Joseph E Flaherty et al. "Software for the parallel adaptive solution of conservation laws by discontinuous Galerkin methods". In: *Discontinuous Galerkin Methods*. Springer Berlin Heidelberg, 2000, pp. 113–123. ISBN: 978-3-642-59721-3. DOI: https://doi.org/10.1007/978-3-642-59721-3_7.

[28] Douglas N. Arnold et al. "Unified Analysis of Discontinuous Galerkin Methods for Elliptic Problems". In: *SIAM Journal on Numerical Analysis* 39.5 (2006), pp. 1749–1779. DOI: https://doi.org/10.1137/S0036142901384162.

[29] H. C. Brinkman. "A calculation of the viscous force exerted by a flowing fluid on a dense swarm of particles". In: *Flow, Turbulence and Combustion* 1.1 (1949). DOI: https://doi.org/10.1007/BF02120313.

[30] Richard Courant. "Variational methods for the solution of problems of equilibrium and vibrations". In: *Bulletin of the American mathematical Society* 49.1 (1943). DOI: https://doi.org/10.1090/S0002-9904-1943-07818-4.

[31] Ray Clough. "The finite element method in plane stress analysis". In: *Proceedings of 2nd ASCE Conference on Electronic Computation, Pittsburgh Pa., Sept. 8 and 9, 1960* (1960).

[32] K. K. Gupta and J. L. Meek. "A brief history of the beginning of the finite element method". In: *International Journal for Numerical Methods in Engineering* 39.22 (1996), pp. 3761–3774. DOI: https://doi.org/10.1002/(SICI)1097-0207(19961130)39:22<3761::AID-NME22>3.0.CO;2-5.

[33] J. H. Argyris and S. Kelsey. *Energy Theorems and Structural Analysis*. Springer New York, 1960. ISBN: 978-1-4899-5850-1. DOI: https://doi.org/10.1007/978-1-4899-5850-1.

[34] M. J. Turner et al. "Stiffness and Deflection Analysis of Complex Structures". In: *Journal of the Aeronautical Sciences* 23.9 (1956). DOI: https://doi.org/10.2514/8.3664.

[35] O. C Zienkiewicz and R. L. Taylor. *The finite element method. Volume 1, Basic formulation and linear problems*. McGraw-Hill, 1989. ISBN: 0070841748.

[36] Klaus Gerdes and Dominik Schötzau. "hp-finite element simulations for Stokes flow — stable and stabilized". In: *Finite elements in analysis and design* 33.3 (1999), pp. 143–165. DOI: https://doi.org/10.1016/S0168-874X(99)00018-9.

[37] Paul Houston, Dominik Schötzau, and Thomas P. Wihler. "Energy norm shape a posteriori error estimation for mixed discontinuous Galerkin approximations of the stokes problem". In: *Journal of Scientific Computing* 22–23.June (2005), pp. 347–370. DOI: https://doi.org/10.1007/s10915-004-4143-7.

[38] Paul Houston and Thomas P. Wihler. "An hp-adaptive Newton-discontinuous-Galerkin finite element approach for semilinear elliptic boundary value problems". In: *Mathematics of Computation* 87.1 (2018), pp. 2641–2674. DOI: https://doi.org/10.1090/mcom/3308.

[39] Adam M. Blakey. *PhD First Year Report*. Tech. rep. University of Nottingham, 2021. URL: https://r.blakey.family/phd1.

[40] Daniele Boffi, Franco Brezzi, and Michel Fortin. *Mixed Finite Element Methods and Applications*. Spring Series in Computational Mathematics. Springer Berlin, Heidelberg, 2013. ISBN: 978-3-642-36519-5. DOI: https://doi.org/10.1007/978-3-642-36519-5.

[41] A.R. Terrel et al. "Automated FEM discretizations for the Stokes equation". In: *BIT Numerical Mathematics* 48.389 (2008). DOI: https://doi.org/10.1007/s10543-008-0178-8.

[42] Paolo Antonietti et al. *AptoFEM user manual v4.0*. Version 4.0.568. 2022.

[43] Patrick R. Amestoy et al. "A Fully Asynchronous Multifrontal Solver Using Distributed Dynamic Scheduling". In: *SIAM Journal on Matrix Analysis and Applications* 23.1 (2001). DOI: https://doi.org/10.1137/S0895479899358194.

[44] A.K. Nanaev et al. "The Human Placenta is Encircled by a Ring of Smooth Muscle Cells". In: *Placenta* 21.1 (2000). DOI: https://doi.org/10.1053/plac.1999.0455.

[45] Denis. Le Bihan. "What can we see with IVIM MRI?" In: *NeuroImage* 187.September 2017 (2019). DOI: https://doi.org/10.1016/j.neuroimage.2017.12.062.

[46] Reuben D O'Dea et al. "A multiscale analysis of nutrient transport and biological tissue growth in vitro". In: *Mathematical medicine and biology: a journal of the IMA* 32.3 (2014), pp. 345–366. DOI: https://doi.org/10.1093/imammb/dqu015.

[47] Ulrich Hornung and Willi Jäger. "Diffusion, convection, adsorption, and reaction of chemicals in porous media". In: *Journal of Differential Equations* 92 (2 1991). DOI: https://doi.org/10.1016/0022-0396(91)90047-D.

[48] Frans N. van de Vosse and Nikos Stergiopulos. "Pulse Wave Propagation in the Arterial Tree". In: *Annual Review of Fluid Mechanics* 43.1 (2011). DOI: https://doi.org/10.1146/annurev-fluid-122109-160730.

A. Summary of Training

All 30 credits are completed, and completed some Researcher Academy courses:

- MAGIC098: Adaptive Finite Element Methods [10 credits]
- G14UQN: Uncertainty Quantification [20 credits]
- Mind Matters: Looking after your mental wellbeing during your PhD
- Careers Beyond Academia
- Light your fire: Motivational tools for researchers
- Fire Safety Training
- Managing your time as a researcher
- Functional Breathing for Stress Relief
- Looking after your mental wellbeing in uncertain times
- Preparing for the first year progression
- Research integrity

B. Plan for Coming 12 Months

In reality, I expect a lot of these things will happen simultaneously over the next 12 months. However, I will use the following as rough deadlines for these tasks.

October 2022 Investigate the effects of varying permeability throughout placenta domain; investigate effect of varying inlet/outlet conditions on nutrient transport; investigate choice of model in high Reynold number regions.

January 2023 Prepare/work towards paper with George Hutchinson on synthetic MRI; to have made contact with Lopa Leach to validate parameter choices against ex-vivo perfusion experiments.

April 2023 To have used moving mesh and FSI methods to model the 'utero-placental' contractions; limited 3D simulations.

July 2023 To have decided the main structure of the thesis and work plan — the core of 2 chapters and introduction should be present, at a minimum.